ACS APPLIED NANO MATERIALS

www.acsanm.org Article

Mesoporous Silica–Fe_3O_4 Nanoparticle Composites as Potential Drug Carriers

Danilo Waismann Losito, Daniele Ribeiro de Araujo, Vinícius Danilo Nonato Bezzon, Pedro Leonidas Oseliero Filho, Fernando Luiz Affonso Fonseca, Camila dos Santos Chagas, Emerson Barbosa, Cristiano Luis Pinto Oliveira, Marcia Carvalho de Abreu Fantini, Fabio Furlan Ferreira, Tereza da Silva Martins,* and Paula Silvia Haddad

Cite This: *ACS Appl. Nano Mater.* 2021, 4, 13363–13378 Read Online

ACCESS | Metrics & More | Article Recommendations | Supporting Information

Downloaded via UNIV OF SAO PAULO on April 1, 2022 at 19:08:07 (UTC).
See https://pubs.acs.org/sharingguidelines for options on how to legitimately share published articles.

ABSTRACT: This work is an innovative study of ordered mesoporous silica (SBA-15) nanocomposites, with different morphologies, and superparamagnetic iron oxide nanoparticles (SPIONs), as promising drug delivery vehicles guided by magnetization. Incorporating SPIONs into SBA-15 is of great interest because it can improve controlled delivery of drugs as well as avoid agglomeration of the nanoparticles. SPIONs were prepared by coprecipitation and thermal decomposition methods and incorporated into SBA-15, with different morphologies, by the incipient wetness impregnation method. The nanocomposites (SBA-15:SPIONs) were characterized by physicochemical techniques, including small-angle X-ray scattering, X-ray diffraction, nitrogen adsorption–desorption isotherms, scanning and transmission electron microscopies, energy-dispersive spectroscopy, magnetization measurements, pair distribution function analysis, Fourier transform infrared spectroscopy, thermogravimetric analysis, and differential thermal analysis. The X-ray diffraction and small-angle X-ray scattering data of the nanocomposites verified that the crystalline phase of magnetite (Fe_3O_4) and the pore structure of the SBA-15 did not undergo significant changes. N_2 physisorption data evidenced significant changes in the textural properties of the pure SBA-15, indicating the incorporation of SPIONs into the mesopores, with greater incorporation when the nanoparticles are obtained by thermal decomposition, in agreement with the small-angle X-ray scattering results. Transmission electron microscopy images, energy-dispersive spectroscopy, and thermogravimetry results evidence the successful incorporation of SPIONs into the silica matrix. The SBA-15:SPIONs presented superparamagnetic behavior. The pair distribution function method revealed a significant variation in the local structure related to changes in the Si–Si–O coordination caused by the decrease in the SBA-15 particle size. The incorporation of SPIONs was better for silica with smaller particle sizes and a higher proportion of SPIONs. Biological assays, such as myelotoxicity and cell viability, demonstrated that the nanocomposites could be safe potential drug delivery vehicles.

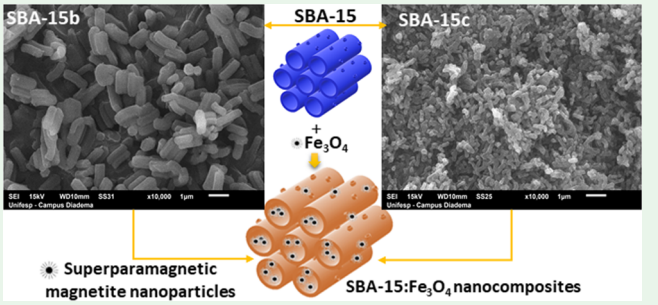

KEYWORDS: *SBA-15 nanocomposites, structural and morphological properties, Fe_3O_4 nanoparticles, magnetization, pair distribution function*

1. INTRODUCTION

Superparamagnetic iron oxide nanoparticles (SPIONs) have several potential applications in different areas, such as catalysis,[1,2] environmental remediation,[3] and biomedicine. They could have a wide variety of therapeutic, diagnostic, and theranostic uses due to their magnetic and biocompatible properties and large surface-to-volume ratios, which allows the addition of clinically relevant drug concentrations on their surface.[4−8]

Nanosized magnetite (Fe_3O_4) or maghemite (γ-Fe_2O_3) particles have been synthesized by our group through coprecipitation and thermal decomposition methods.[9−12] The latter approach has the advantage of producing smaller nanoparticles with better homogeneous distribution.[6,12] They exhibit superparamagnetic behavior when the temperature is increased above the blocking temperature (BT), acting as a single magnetic domain. This individual nanoparticle has a high magnetic moment and behaves like a giant paramagnetic atom, quickly responding to the applied magnetic fields with

Received: September 9, 2021
Accepted: November 24, 2021
Published: December 6, 2021

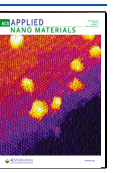

ACS Publications © 2021 American Chemical Society

negligible residual magnetism and coercivity.[6,11] However, a high iron concentration in the body affects cell viability, causes oxidative stress, and has possible toxicities, including cardiac and hepatic toxicity.[4−6] Surface functionalization of SPIONs with biocompatible compounds such as ordered mesoporous silica (OMS) is a useful approach to avoid nanoparticle agglomeration, thus allowing the conjugation with therapeutic molecules (drugs and bioactive compounds).[13−15]

OMSs have been studied for drug delivery, catalysis, adsorption, cosmetics, and especially biomedical applications.[16−25] OMSs, including SBA-15, have unique structural and textural properties advantageous for biomedical applications. Among these advantages are low toxicity; good biocompatibility; thermal, hydrothermal, mechanical, and chemical stabilities; ordered mesoporosity; high surface area (around 900 $m^2\ g^{-1}$); pore volume ranging from 1 to 5 $cm^3\ g^{-1}$; adjustable pores (2−50 nm); narrow pore size distribution (PSD); and easy surface functionalization due to a large number of silanol groups (Si−OH) on the silica surface. Due to these characteristics, especially structural and textural (pore size, pore volume, and wall thickness) properties, SBA-15 has become more important for biomedical applications, as drug delivery systems, than other silica-based structures, including MCM-41 and silica-gel, because SBA-15 presents thicker walls and larger pore diameter and pore volume than the analogous MCM-41, that also has a hexagonal structure (*p6mm*). Consequently, SBA-15 has higher mechanical stability and greater adsorption and release ability of drugs. For these reasons, the SBA-15 was chosen as a silica matrix in this study.[16,17,21,23]

Silica-based nanocomposites have been synthesized by several synthesis methodologies. The resulting materials exhibited better physical and chemical properties than pure materials.[19,20,22,23] Jardim et al.[19,22] synthesized and characterized SBA-15:TiO_2 nanocomposites by postsynthesis and direct synthesis methods, varying some synthesis parameters, such as the reaction media. These strategies formed nanocomposites with different morphological and structural properties, thus enabling their use in photocatalysis and sun protection applications due to the phase selectivity (anatase and rutile, respectively). Vieira et al.[20] also prepared SBA-15:ZnO nanocomposites, and these materials exhibited a higher sun protection factor (SPF) than pure ZnO.

Iron oxide nanoparticles−mesoporous silica nanocomposites have been prepared by different methodologies for potential applications in catalysis and biomedicine.[7,14,23,26−28] Souza et al.[28] reported magnetite-SBA-15 nanocomposites for drug release systems, and their *in vitro* assays revealed that the constant magnetic field has little influence on drug release. However, the low-frequency alternating magnetic field had a significant influence on the drug release profile. These results were attributed to a possible drug-nanoparticle interaction and the confinement into silica mesopores.

Kim et al.[29] studied Pd-containing and γ-Fe_2O_3 superparamagnetic nanoparticles porous silica nanocomposites for the catalysis of 4-nitrophenol to 4-aminophenol, obtaining better results than the commercial Pd under identical synthesis conditions. In this study, their silica avoided agglomeration and provided stability to the nanocomposite, preventing loss of catalytic efficiency.

In all cases, silica offers stability to the species, making the systems very promising for their respective applications. Although several scientific studies have been published on iron oxide nanoparticles and SBA-15 composites, as far as we know, no studies have reported nanocomposites based on SBA-15 and magnetite prepared by different methodologies, comparing their textural and morphological properties, as well as their local atomic structure, as will be explored herein. This approach is important to select the more adequate characteristics of these nanocomposites for each specific use since morphology, size, and colloidal stability are essential for modulating their performance.

Porosity, pore structure, as well as size and shape morphology of the silica particle must be controlled for applications in several areas, including catalysis, separation, and biomedicine.[13] In biomedicine, the particle size and shape can be influenced by numerous biological processes such as biocompatibility, biodistribution, and toxicity. The particle size can affect the drug release, absorption, and biodistribution.[8,13] Therefore, it is important to control the morphological and structural properties of these materials.

This paper reports the preparation and characterization of SBA-15-based nanocomposites, with different particle morphologies and magnetite concentrations, obtained by coprecipitation and thermal decomposition methods. This study aimed to compare the magnetic, textural, structural, and morphological properties of different superparamagnetic nanocomposites and their local atomic structure using pair distribution function (PDF) analysis.

Although studies involving nanocomposites of SBA-15 and iron nanoparticles have already been carried out, none have been reported for SBA-15:Fe_3O_4 nanocomposites with different particle morphologies and comparison of iron nanoparticles prepared by different methodologies, as shown here. Additionally, we present an innovative study using distribution function (PDF) analysis for these materials.

The X-ray total scattering technique and the pair distribution function method have been applied in several structural analyses about the possibility of highlighting local structural ordering. The PDF method yields the distance distribution of atomic pairs, providing a pattern of interatomic interactions in real space.[30] Therefore, this method can be used to describe amorphous and nanocrystalline structures for inorganic or organic materials.[30−33]

Rantanen et al.[34] described the amorphous SBA-15 structure obtained with different pore sizes using the PDF method with data from a laboratory X-ray powder diffractometer. The authors noticed that the aging temperature during the synthesis of amorphous SBA-15 rendered different microporosity levels and local ordering with different wall thicknesses. In the present study, the PDF method was applied (i) to better describe the amorphous structure of silica obtained with different morphologies, highlighting the most significant structural differences reached, (ii) and to verify the influence of the SPION insertion on the SBA-15 amorphous structure and how they are connected to microporosity. Biological assays completed the characterization of the SPIONs to propose their use in medical treatments.

2. EXPERIMENTAL SECTION

2.1. Materials. Tetraethyl orthosilicate [TEOS, $Si(OC_2H_5)_4$, 98%], poly(ethylene glycol)-*block*-poly(propylene glycol)-*block*-poly(ethylene glycol) [Pluronic P123, $HO(CH_2CH_2O)_{20}(CH_2CH(CH_3)O)_{70}(CH_2CH_2O)_{20}H$], oleic acid (OA, $CH_3(CH_2)_7CH = CH(CH_2)_7COOH$, ≥99%), iron(III) acetylacetonate [$Fe(acac)_3$, $Fe(C_5H_7O_2)_3$, 97%], iron(III) chloride hexahydrate ($FeCl_3{\cdot}6H_2O$,

https://doi.org/10.1021/acsanm.1c02861
ACS Appl. Nano Mater. 2021, 4, 13363−13378

Scheme 1. Schematic Illustration of the Synthesis of Superparamagnetic Iron Oxide Nanoparticles (A and B), SBA-15 Pure, and SBA:Fe_3O_4 Nanocomposites (C)

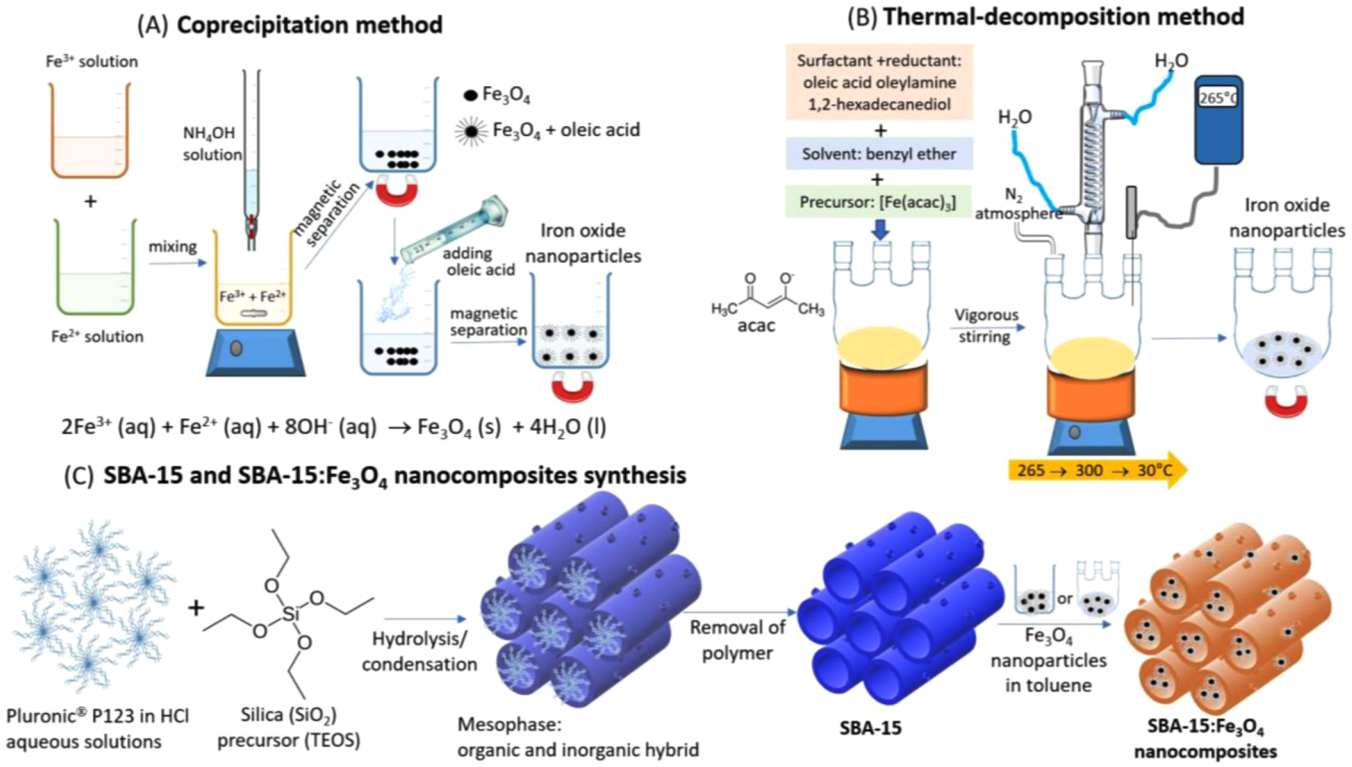

reagent grade, ≥98%), iron(II) chloride tetrahydrate ($FeCl_2{\cdot}4H_2O$, 98%) 1,2-hexadecanediol [$CH_3(CH_2)_{13}CHOHCH_2OH$, technical grade, 90%], benzyl ether [$(C_6H_5CH_2)_2O$, 98%], oleylamine [$CH_3(CH_2)_7CH = CH(CH_2)_7CH_2NH_2$, ≥98%], and toluene ($C_6H_5CH_3$, ≥99.7%) were purchased from Sigma-Aldrich. Hydrochloric acid (HCl, 37%), ammonium hydroxide solution (NH_4OH, 28.0−30.0%), and ethanol (C_2H_6O, 99%) were purchased from Synth, Brazil. All reagents and solvents were used as received without further purification.

2.2. Synthesis of Materials. Scheme 1 shows a schematic illustration of the synthesis of superparamagnetic iron oxide nanoparticles (A and B), SBA-15 pure, and SBA:Fe_3O_4 nanocomposites (C).

2.2.1. Synthesis of Magnetite (Fe_3O_4) Nanoparticles. Magnetite nanoparticles were synthesized by coprecipitation[9] and thermal decomposition[10] methods (Scheme 1), as further described below.

2.2.1.1. Coprecipitation. Two solutions of $FeCl_3{\cdot}6H_2O$ and $FeCl_2{\cdot}4H_2O$ were prepared with HCl (1.0 mol L^{-1}). Then, 4.0 mL of $FeCl_3{\cdot}6H_2O$ acid solution (0.5 mol L^{-1}) and 1.0 mL of $FeCl_2{\cdot}4H_2O$ acid solution (1.0 mol L^{-1}) were mixed and stirred, while a volume of 50 mL of NH_4OH (0.7 mol L^{-1}) was added as a precipitator. The dispersion was magnetically decanted, followed by adding 6 mL of oleic acid (OA) and stirring for 30 min to obtain coated magnetite nanoparticles. The resulting material was washed several times with ethanol and referred to as SPIONCo.

2.2.1.2. Thermal Decomposition. $Fe(acac)_3$ (2 mmol), 1,2-hexadecanediol (10 mmol), benzyl ether (20 mL), oleic acid (6 mmol), and oleylamine (6 mmol) were placed in a reaction flask under continuous N_2 flow with vigorous stirring. Under a nitrogen atmosphere, the mixture was heated to 265 °C for 30 min, followed by further heating at 300 °C for 30 min. The magnetite nanoparticles were purified by precipitation using ethanol (40 mL) and centrifugation (4000 rpm, 20 min) to remove the solvent. The magnetite nanoparticles coated with oleic acid were washed three times with ethanol and dried under reduced pressure. This resulting material was referred to as SPIONT.

2.2.2. SBA-15 Synthesis. SBA-15 samples were synthesized at various temperatures and stirring rates according to the method described by Zhao et al.[23] with minor modification (Scheme 1), as further described: 4 g of Pluronic P123 was dissolved in 120 mL of HCl (2.0 mol L^{-1}) and 30 mL of deionized water under stirring for 1 h at room temperature. The resulting solution was heated and stirred until it reached the temperature synthesis, and then 8.9 mL of TEOS was added dropwise. The mixture was kept in an oil bath at 40, 50, or 70 °C, under vigorous stirring (500, 200, and 500 rpm, respectively), for 24 h and then transferred to a Teflon-lined autoclave and heated at 100 °C for 48 h. The solid was isolated by filtration and dried at 60 °C. The template (Pluronic P123) was removed, combining solvent extraction and calcination. After the solvent extraction using ethanol, the resulting solid was calcined under an air atmosphere at 550 °C for 4 h because the solvent extraction is not efficient for the complete removal of the template. The SBA-15 samples were prepared by varying synthesis temperatures at 40, 70, and 50 °C, referred to as SBAa, SBAb, and SBAc, respectively. The recovered Pluronic P123 was reused in other syntheses of SBA-15.

2.2.3. Preparation of SBA-15:SPION Nanocomposites. All SBA-15:SPION nanocomposites were prepared by the postsynthesis method following the procedure described in the literature with some minor modifications (Scheme 1).[20,22] SBA-15 was activated at 200 °C for 2 h, aiming to eliminate water molecules and then dispersed in toluene. Then, the magnetite nanoparticles (10 and 30 wt %) were added to the SBA-15 dispersion. The resulting mixture was stirred at room temperature for 24 h, and then the solid was isolated and dried by rotary evaporation. The nanocomposites with 30 wt % of iron oxide nanoparticles were prepared only using the SBAa. The obtained nanocomposites were denoted SBAx:FeyCo and SBAxFeyT, where SBAx stands for SBAa, SBAb, and SBAc silicas; Fe = Fe_3O_4 nanoparticles coated with oleic acid; y = 10 and 30 wt % Fe_3O_4 nanoparticles coated with oleic acid; Co = magnetite obtained by coprecipitation method; and T = magnetite obtained by the thermal decomposition method. The mass ratio of SBA-15 to Fe_3O_4 nanoparticles coated with oleic acid was 1:0.1 for SBAxFe10Co and

https://doi.org/10.1021/acsanm.1c02861
ACS Appl. Nano Mater. 2021, 4, 13363−13378

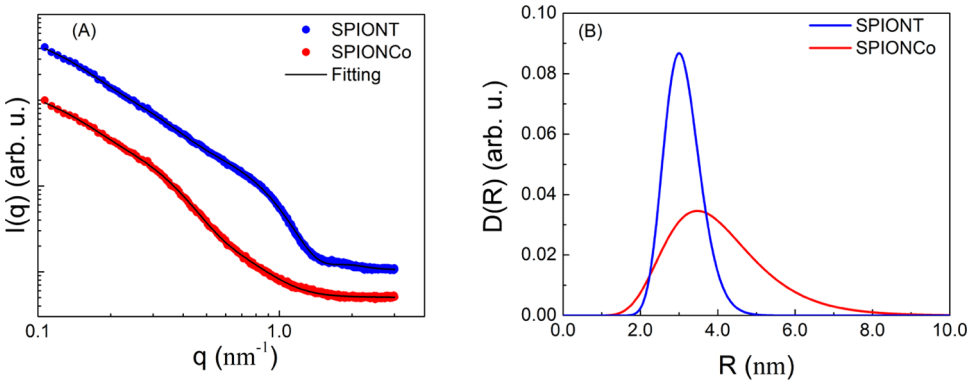

Figure 1. (A) Small-angle X-ray scattering (SAXS) data (filled circles) about powder samples superparamagnetic iron oxide nanoparticles (SPIONs) fitted with the model briefly described in the text and detailed in the Supporting Information (continuous lines). The SAXS profiles were vertically shifted in scale for clarity. (B) Normalized size distributions, i.e., $\int D(R)\mathrm{d}R = 1$, for the parameter R (radius of the particles) obtained from the fittings of each SPION investigated in this work.

SBAxFe10T and 1:0.3 for SBAaFe30Co. The mass ratio of SBA-15 to toluene was 1:0.035.

2.3. Characterization. Small-angle X-ray scattering (SAXS) measurements were performed using a Nanostar (Bruker) instrument equipped with a microfocus Genix 3D system (Xenocs). The powder samples were placed in a sample holder between two mica slices, and the scattered intensity was collected on a two-dimensional (2D) Vantec-2000 detector. The sample-to-detector distance was ∼67 cm, which provided an effective range of the modulus of the transfer moment vector q experimentally accessible of 0.1−3.0 nm^{-1}, with $q = 4\pi \sin(\theta)/\lambda$ (where 2θ is the scattering angle and λ = 0.15418 nm is the X-ray wavelength from the Cu Kα radiation). All data were normalized by the measuring time and corrected for absorption effects. The collected intensities were corrected using background scattering (from mica slices) and sample transmission. For data treatment, the SUPERSAXS package was used.[35] The data analysis was performed using the models described in the Supporting Information.

Adsorption−desorption isotherms (named NAI) were performed with a Quantachrome (NOVA 1200e) porosimeter at 77 K using nitrogen of 99.998% purity. Prior thermal treatment at 100 °C for 6 h was performed to dry the samples, and the isotherms were taken at 77 K using nitrogen with 99.9998 purity. The specific surface area was evaluated using the Brunauer−Emmet−Teller (BET) method,[36] and the pore volume and pore size distribution (PSD) were calculated using the Barrett−Joyner−Halenda (BJH) method.[37]

Fourier transform infrared (FTIR) spectra were recorded in the range 4000−400 cm^{-1}, using an Agilent Cary 630 FTIR spectrometer. IR measurements were performed in attenuated total reflection (ATR) mode.

Scanning electron microscopy (SEM) images and energy-dispersive spectrometry (EDS) measurements were made on a JEOL microscope, model JSM 6610LV, operating with a secondary electron imaging (SEI) detector. The samples were placed on conductive double-sided adhesive carbon tape and covered with a thin layer of gold.

For transmission electron microscopy (TEM) analysis, the samples were dispersed in ethanol and dried on the carbon-coated copper grid. Images were acquired using a JEOL JEM-2100, operating at 200 kV acceleration voltage and beam current at 102 μA. The SPION size was directly obtained from TEM analysis by JEOL 20100 Viewer software.

Thermogravimetric analysis (TGA) and differential thermal analysis (DTA) were done using a Shimadzu DTG-60H thermobalance in the temperature range from room temperature (25 °C) to 900 °C with a heating rate of 10 °C min^{-1}, under dynamic air atmosphere (50 cm^3 min^{-1}), using platinum crucibles with ca. 5 mg of samples.

Magnetization measurements were performed using a SQUID (superconducting quantum interference device) magnetometer (Quantum Design, San Diego, CA, USA). The powder samples were slightly pressed and conditioned in a cylindrical lucite holder. The magnetization measurements were performed in both zero-field-cooling (ZFC) and field-cooling (FC) modes.

X-ray total scattering analyses were performed at room temperature using a high-resolution diffractometer model STADI-P from STOE (Darmstadt, Germany) in transmission geometry by employing Mo Kα_1 radiation (λ = 0.7093 Å) with the sample loaded in 1 mm diameter special glass 14 capillaries (Hilgenberg, Malsfeld, Germany). The data were collected by a silicon detector Mythen 1K (Dectris, Baden, Switzerland), in the range of 4.0−136.2° (2θ) with a step size of 0.015° and 100 s of integration time at each 0.785°, reaching a maximum Q-value of ∼16.4 Å^{-1}. An average of four patterns for each sample was obtained to accurately measure the counting statistics and model the background and sample holder absorption; the empty capillary was also measured under the same conditions. The pair distribution function (PDF) patterns were obtained using the PDFGetX3[38] software that uses an *ad hoc* data correction method, where the parameters of the multiplicative and additive corrections are varied using a regression method to yield an accurate structure function. The total structure function $S(Q)$ can be obtained from the intensity on a per-atom scale $I(Q)$ and the form factor f as follows

$$S(Q) = \frac{I(Q) - [\langle f^2(Q)\rangle - \langle f(Q)\rangle^2]}{\langle f(Q)\rangle^2} \quad (1)$$

where $S(Q)$ is Fourier transformed into the PDF and

$$G(r) = \frac{2}{\pi}\int_{Q_{min}}^{Q_{max}} Q[S(Q) - 1]\sin(Qr)\mathrm{d}Q \quad (2)$$

The same data were used to perform Rietveld refinements—using the TOPAS-Academic v.6[39] software—taking into account the magnetite crystal structure for the composite samples.

2.4. Biological Assays. *2.4.1. Myelotoxicity Assays.* The blood samples used are from healthy human samples from the Clinical Laboratory at the University Health Center of ABC, Brazil.

The biological assays evaluated the cytotoxicity of the pure nanomaterials SBA-15, SPIONs, and nanocomposites SBA:Fe_3O_4. Hematological analyses were performed by blood tests on XN-1000 (Roche) using the flow cytometry method. The sample preparation was composed of 100 μL of the analyzed compound and 1000 μL of total blood. Then, the sample was homogenized and then analyzed.

2.4.2. Cell Viability of Lymphocytes Assays. The used samples were collected according to good laboratory practices from the Clinical Laboratory Analysis of the University Health Center of ABC, Brazil, from a healthy donor. For the analysis, peripheral blood collected in the K_3EDTA vacuum tube was used. The viability was

https://doi.org/10.1021/acsanm.1c02861
ACS Appl. Nano Mater. 2021, 4, 13363−13378

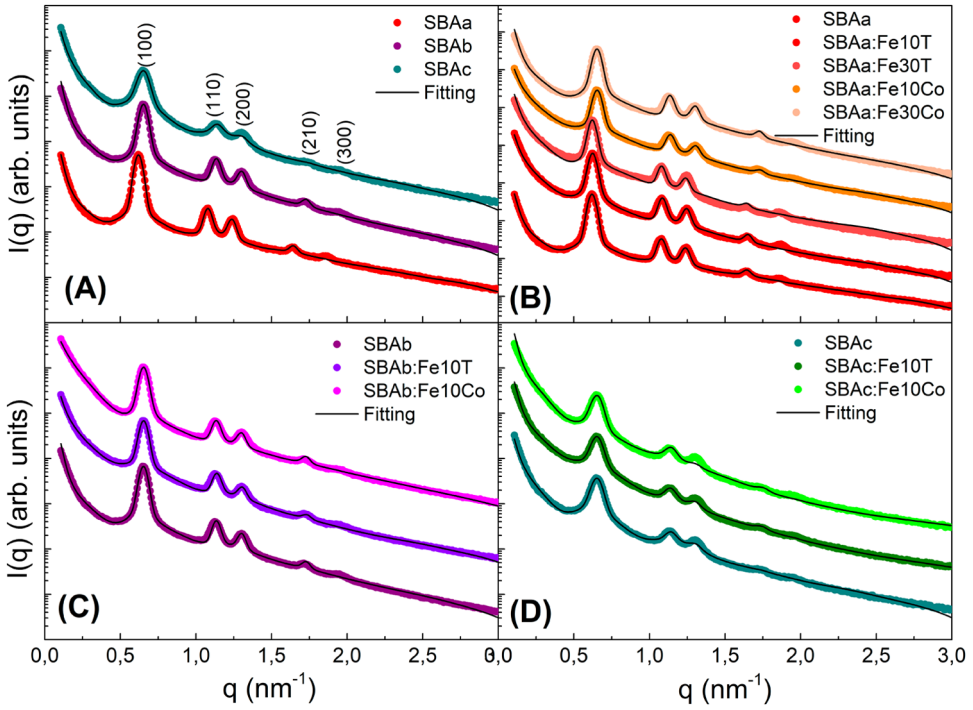

Figure 2. Small-angle X-ray scattering (SAXS) data (filled circles) of SBA-15 syntheses (A) and SBA-15 + SPIONs (B–D) fitted by the models described in the text and detailed in the Supporting Information (continuous lines). The SAXS profiles were vertically shifted in scale for clarity. The Miller indices assigned to two-dimensional hexagonal mesoporous structure (*p6mm*) like SBA-15 are shown in (A).

assessed by the MTT—methyl-thiazolyl-tetrazolium—method (a colorimetric assay to assess cellular metabolic activity) using 3-bromide(4,5-dimethylthiazol-2-yl)-2,5-diphenyltetrazolium SIGMA. The compounds were analyzed at concentrations of 2000, 1000, 250, 62.5, 5, and 0.1 $\mu g{\cdot}mL^{-1}$. To separate the mononuclear fraction, the Ficoll Hypaque technique was employed. The Neubauer chamber was utilized to count and obtain the final concentration of 1×10^5 cells mL^{-1}. The cells were added to the Dulbecco's modified Eagle's medium (DMEM) as culture medium (200 μL), and 20 μL of each compound was added to the plate's wells.

In addition, the cells were incubated for 24 h in an oven at 37 °C in a 5% CO_2 atmosphere and 100 μL of MTT solution in phosphate-buffered saline (0.5 $mg.mL^{-1}$) was added per well of the plate. The cells were incubated for 2 h at 37 °C, and after adding 200 μL of pure dimethyl sulfoxide (DMSO), the plate was shaken for 3 min until the formazan crystals disappeared. After coloring, the absorbance was measured at 540 nm in the Adaltis Labotech equipment.

2.4.3. Statistical Analysis. Statistical analyzes were performed using GraphPad Prism software. All variables were analyzed descriptively, and measurements of central tendency indicated the quantitative values. The analysis of variance (ANOVA) test was applied. The results were analyzed with a significance level of 5% ($p \leq 0.5$).

3. RESULTS AND DISCUSSION

3.1. Size Distribution of the SPIONs. The SAXS curves for powdered SPION samples are shown in Figure 1A (filled circles). The simple model (see the Supporting Information for more details) considers a spherical shape for the SPIONs and a log-normal distribution $D(R)$ for the particle radius R to obtain information about nanoparticle size distribution. As a result, it was possible to obtain the average radius R_0 and its standard deviation σ_0. Furthermore, a term following the Guinier law was included to consider the nanoparticle clusters (i.e., aggregates of nanoparticles) primarily responsible for the observed scattering at low q. After several tests, we realized that it was necessary to have two radii of gyration, R_{G_1} and R_{G_2}, to satisfactorily describe the scattering at a low q. In the model, the sum over all percentual contributions of each term to the total scattering, f_i, was evaluated so that $\sum f_i = 1$. The fittings, both satisfactorily adjusted, are shown in Figure 1A (continuous lines), whereas the size distributions obtained are depicted in Figure 1B. The values of the fitting parameters are summarized in Table S1.

The size distributions for SPIONCo (coprecipitation method) are, on average, larger and more polydispersed than SPIONT (thermal decomposition method). The values obtained for R_0 and σ_0 are consistent with the literature and not only represent crucial information about the possibility of SPION encapsulation into the SBA-15 mesopores but also elucidate one of the main differences between the synthesis methods, which is the better control of size and polydispersity for thermal decomposition.[40]

The nanoparticle clusters have, in both cases, the radii of gyration of ~7.0 and 16.0 nm. If these agglomerates have a spherical shape, their radii are given by $R = \sqrt{\frac{5}{3}} R_g$. Thus, the calculation of cluster radius gives ~9.0 and 19.0 nm. Although these clusters will not enter the mesopores, they could stay trapped on the silica surface, as suggested by TEM images presented herein, and, consequently, prevent smaller particles from entering the mesopores. The SPION scattering contributes a low percentage of the total scattering (~5% for SPIONT and ~2% for SPIONCo) compared with the cluster scattering. This result is expected because the scattered intensity is proportional to the square of the particle volume. Thus, larger particles are more prominent to the total scattering, even if they are not numerous in the sample.[41]

3.2. SBA-15 and SBA-15 + SPIONs. SAXS curves of the calcined samples of pure SBA-15 (SBAa, SBAb, and SBAc) and

https://doi.org/10.1021/acsanm.1c02861
ACS Appl. Nano Mater. 2021, 4, 13363–13378

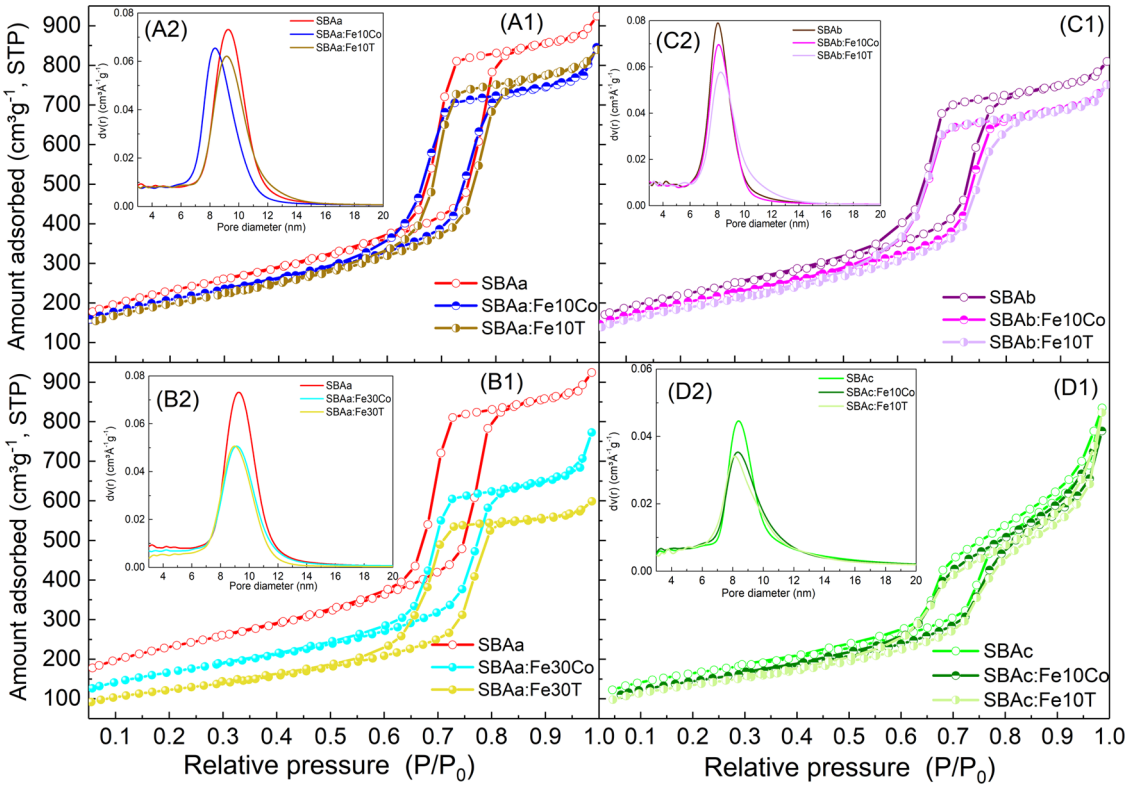

Figure 3. Nitrogen adsorption/desorption isotherms for pure SBA-15 samples and SBA-15:Fe_3O_4 nanocomposites (A1−D1). The insets show adsorption pore size distribution by the BJH method for all materials (A2−D2).

SBA-15:Fe_3O_4 nanocomposites are in Figure 2. In Figure 2A, the nanocomposites display well-ordered mesoporous phases and have five well-defined diffraction peaks that correspond to the (*hkl*) Miller indices (100), (110), (200), (210), and (300), which are assigned to a two-dimensional hexagonal mesoporous structure (*p6mm*), typical of pure SBA-15, as described in the literature.[21] Comparing the SBAb and SBAc silica samples with SBAa prepared by a conventional method reported by Zhao et al.,[23] we observed that the combination of temperature (50 and 70 °C) and stirring rate (200 and 300 rpm, respectively) promoted a peak shift to higher q values in the SAXS curves of the samples SBAb and SBAc. This behavior corresponds to lower interplanar distances (characterized by the lattice parameter a), which are related to shrinkage of mesopores, in agreement with the nitrogen adsorption isotherm (NAI) results. These peak shifts can be assigned to the increased polymerization degree, in which Si−OH groups form Si−O−Si bonds due to rising temperatures.[42−45]

The SAXS curves of SBA-15:Fe_3O_4 nanocomposites are shown in Figure 2B−D. For all of them, the characteristic reflections [(100), (110), (200), (210), and (300)] from pure SBA-15 have been preserved after the incorporation of SPIONs, indicating that the silica exhibits high mechanical stability. Nevertheless, the decrease in the peak intensity in the curves of SBA-15:Fe_3O_4 nanocomposites indicates nanoparticle incorporation and a change in the curves for q < 0.05 Å, probably due to nanoparticle clusters on the silica surface.

We analyzed the data with a previously used model,[46,47] with minor changes detailed in the Supporting Information to obtain quantitative information on the mesopore structure of the silica and how incorporating the nanoparticles alters it. The right fittings are presented in Figure 2 (continuous lines), while the parameter values are summarized in Table S2 together with their meaning.

One important piece of information obtained from the fittings is the indication of nanoparticle incorporation inside the mesopores. From the size distributions shown in Figure 1B, the radii of SPIONT and SPIONCo are in the ranges of approximately 2.0−5.0 and 1.5−8.5 nm, respectively. Therefore, considering the range of mesopore diameter values for pure SBA-15, we conclude that some fraction of the nanoparticles could enter the mesopores. This hypothesis is corroborated by the values of parameter B, linked to the electronic density contrast of core and shell of the cylindrical mesopores, as detailed in the Supporting Information, and able to indicate if the mesopore is "empty" (B = 1) or not (B < 1). Hence, according to the B values shown in Table S2, pure SBA-15 has empty mesopores, as expected, different from SBA-15:Fe_3O_4 nanocomposites. For them, we observe that R, T, and σ did not exhibit significant variations compared to the pure SBA-15 or the lattice parameter a. The SAXS results are a combination of empty and filled mesopore contributions to the scattering intensity.

For the other parameters, σ_a allows us to distinguish the ideal (σ_a = 0) from the nonideal 2D-hexagonal lattice. In all analyzed curves, we observed nonideal lattices, and the values of σ_a varied from 0.0024 to 0.0067 nm. Some curves have a higher slope at low q values, less than 0.5 nm^{-1}, compared to pure SBA-15 curves, and this is attributed to the presence of nanoparticle clusters on the silica surface. In addition to the clusters with $R_{G_2} \sim 16.0$ nm, always present in the model (see the Supporting Information), in some cases, it was necessary to include the adjustable parameter R_{G_1}, as shown in Table S2 (the cases where R_{G_1} was not needed were indicated as "-"),

https://doi.org/10.1021/acsanm.1c02861
ACS Appl. Nano Mater. 2021, 4, 13363−13378

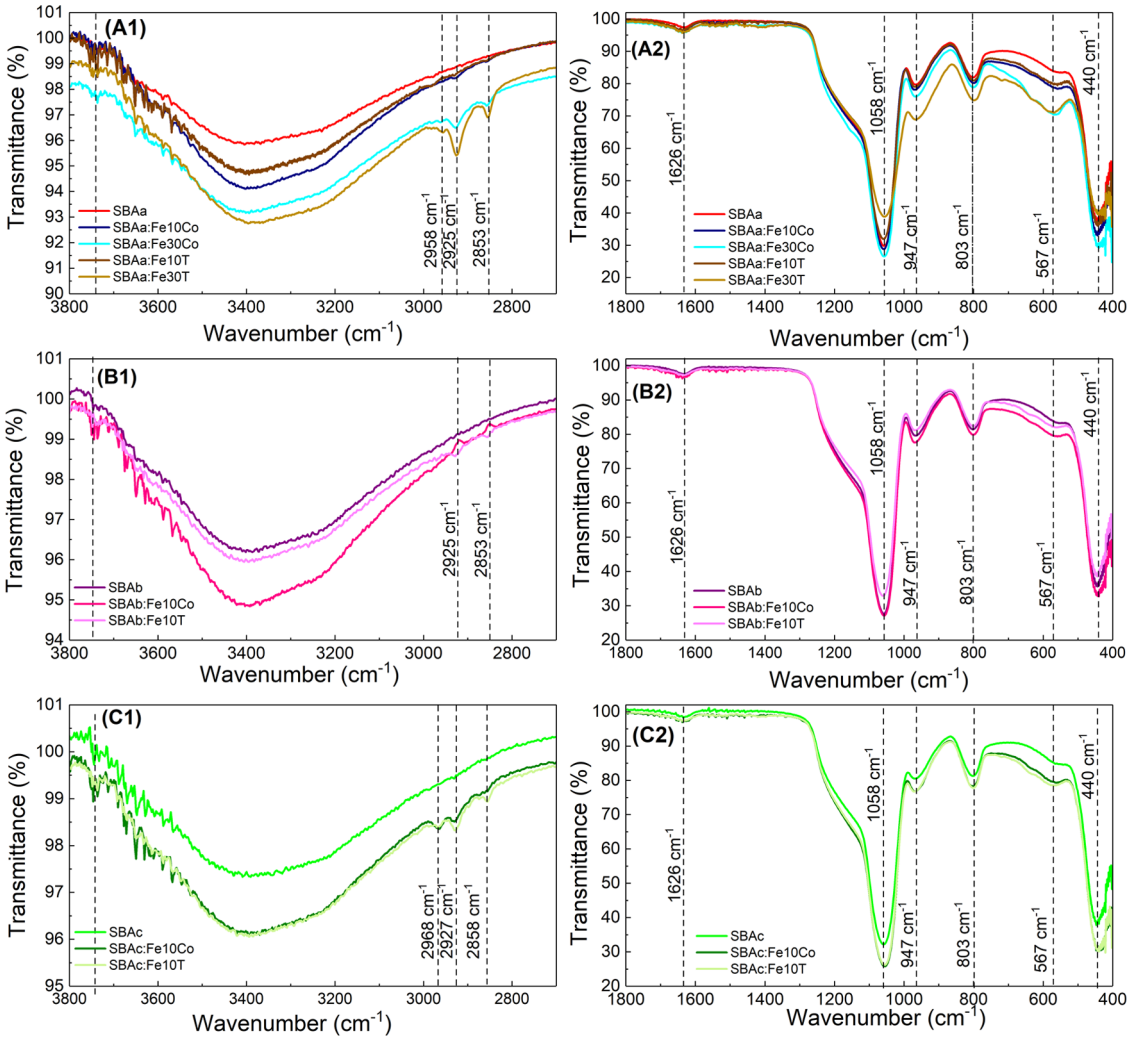

Figure 4. Fourier transform infrared spectra of pure SBA-15 samples (SBAa, SBAb, SBAc) and SBA-15:Fe_3O_4 nanocomposites. (A1, A2): SBAa:FeyCo and SBAa:FeyT (y = 10 and 30 wt % of Fe_3O_4 nanoparticles); (B1, B2): SBAb:Fe10Co and SBAb:Fe10T; and (C1, C2): SBAc:Fe10Co and SBAc:Fe10T.

which varied in the range of 3.0−10.0 nm, thus providing information about nanoparticle clusters in the presence of silica, complementing the characterization performed in the previous section on just nanoparticle clusters. According to the higher temperatures used in their syntheses, the lattice parameters of the SBA(b,c) samples are slightly smaller than SBAa. Comparing the B values of the complexes in Table S2 suggests that the efficiency of encapsulation in the sample SBAa is higher for the T method than for the Co method. This result is in agreement with the NAI data. Furthermore, the encapsulation yield of the T method increased together with the SPIONs concentration. This is an expected result since the size distribution of the SPIONs presented a smaller mean radius and is less spread in the T method.

On the other hand, the B values of samples SBA(b,c) with the same SPION concentration showed that the Co method is more efficient than the T one since the B values are lower for the Co synthesis strategy. This result contradicts the NAI ones, which found a more considerable decrease in the samples' surface area obtained by the T method. In this case, modifications in the silica morphology may explain this unexpected result because smaller particles can fill the short silica rods more easily. Furthermore, the changes in the morphological distribution in the entrance of the mesopore interfere in their blocking.

3.3. N_2 Adsorption/Desorption Isotherms (NAI). Figure 3A1−D1 presents the N_2 adsorption/desorption isotherms of pure SBA-15 samples and SBA-15:Fe_3O_4 nanocomposites, and the insets (A2−D2) show the adsorption pore size distribution by the BJH method for all materials. Table S3 lists the textural properties obtained from N_2 adsorption/desorption isotherms.

According to the IUPAC classification, all physisorption isotherms are of type IV and exhibit H1 hysteresis loops[48] and are characteristic of hexagonal cylindrical channel mesoporous materials, such as SBA-15, with a pore size of about 10 nm, as reported in the literature.[21,49] Comparing the physisorption isotherms of SBA-15 samples (SBAa, SBAb, and SBAc) elucidates that the shape of the isotherms of SBAb and SBAa is very similar, although the latter has more adsorbed N_2 than SBAb. According to the specific surface area, it decreased as the synthesis temperature increased. For both samples (SBAa and SBAb), the adsorption branch of the isotherm had a sharp inflection at P/P_0 between 0.57 and 0.81, characteristic of capillary condensation within uniform pores corroborating with SAXS analysis that showed the formation of an ordered mesoporous structure. Although the SBAc sample also

https://doi.org/10.1021/acsanm.1c02861
ACS Appl. Nano Mater. 2021, 4, 13363−13378

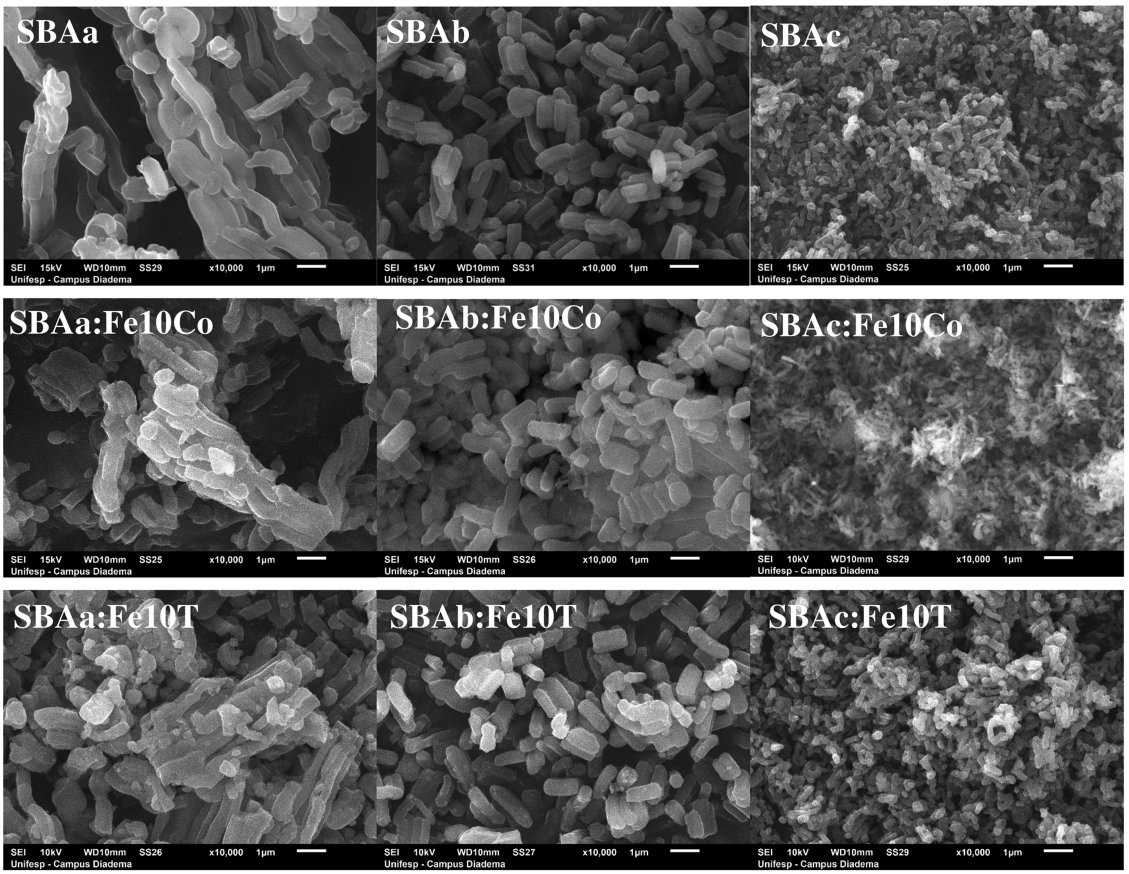

Figure 5. Scanning electron microscopy images of SBA-15 samples (SBAa, SBAb, and SBAc) and SBA-15:Fe_3O_4 nanocomposites (SBAa:Fe10Co, SBAb:Fe10Co, SBAc:Fe10Co, SBAa:Fe10T, SBAb:Fe10T and SBAc:Fe10T).

exhibited a type-IV isotherm, the inflection was slightly shifted to higher pressures at P/P_0 = 0.60−0.84. The plateau of the sorption isotherms, attributed to the capillary pressure, is also lower, indicating that the mesoporous volume and surface area were less than the other two silicas (SBAa and SBAb).

A narrow pore size distribution was obtained using the adsorption isotherm of SBA-15 samples (Figure 3A2,C2,D2); however, the pore diameter decreases with increasing synthesis temperature, from 40 °C (SBAa) to 50 °C (SBAc) and 70 °C (SBAb), corroborating with SAXS results, but the pore wall thickness increased (Table S3).

The nanocomposites (SBA-15:SPIONs) have an isotherm profile similar to the SBA-15 samples. However, the amount of N_2 adsorbed in the nanocomposites decreased compared to the pure SBA-15 samples. The specific surface area and pore volume of nanocomposites (Table S3) also decreased compared to pure silica. The results obtained indicate that the nanoparticles were incorporated into the silica pores. The decrease in the specific surface area is more pronounced as the nanoparticle content increases in the nanocomposites and for the samples prepared by the thermal decomposition method due to their smaller particle size, which favors their incorporation into the mesopores. On the other hand, the inclusion of nanoparticles led to increased silica wall thickness (Table S3), suggesting the deposition of these nanoparticles in the silica walls.

3.4. Fourier Transform Infrared (FTIR) Spectra. Figure 4 presents the FTIR spectra of pure SBA-15 samples and SBA-15:Fe_3O_4 nanocomposites. Typical bands assigned to silica vibrational modes were observed in all samples, with the significant shift of these bands, suggesting that the iron nanoparticles interact only slightly with the silica. A weak band at 3740 cm^{-1} is attributed to the free silanol groups (Si−OH), and the broad band at ca. 3000−3700 cm^{-1} is attributed to O−H stretching (νOH) of adsorbed water molecules and silanol groups. The band observed at 1626 cm^{-1} corresponds to the H−O−H bending ($\delta_{H\text{-}O\text{-}H}$). The broad band between 3000 and 3700 cm^{-1} and the H−O−H bending indicate adsorbed water in silicas and nanocomposites.[26] The asymmetric and symmetric vibrations of siloxane groups (Si−O−Si) appear at 1058 cm^{-1} [ν_{as}(Si−O−Si)], 947, and 803 cm^{-1} [ν_s(Si−O−Si)], and the bending vibration from Si−O−Si ($\delta_{Si\text{-}O\text{-}Si}$) is observed at 440 cm^{-1}.[22,26] The Fe−O stretching vibration mode at ca. 570 cm^{-1} from Fe_3O_4 nanoparticles is more pronounced with a large amount (30 wt %) of nanoparticles in the nanocomposites.[7]

Three vibration bands observed at 2960, 2930, and 2850 cm^{-1} in the SBA-15:Fe_3O_4 nanocomposites are characteristic of C−H (ν_{as} and ν_s) stretching modes of the long aliphatic chains of oleic acid.[50] The presence of oleic acid increases as the amount of Fe_3O_4 nanoparticles coated with oleic acid in the nanocomposites increases (from 10 to 30 wt %), evidencing the incorporation of magnetite nanoparticles in the silica matrix.

3.5. Scanning Electron Microscopy (SEM) and Energy-Dispersive Spectroscopy (EDS). SEM images (Figure 5) show the morphology of pure SBA-15 samples prepared by different synthesis temperatures and SBA-15:Fe_3O_4 nanocomposites prepared with 10 wt % of iron nanoparticles. The different SBA-15 synthesis procedures resulted in a different

https://doi.org/10.1021/acsanm.1c02861
ACS Appl. Nano Mater. 2021, 4, 13363−13378

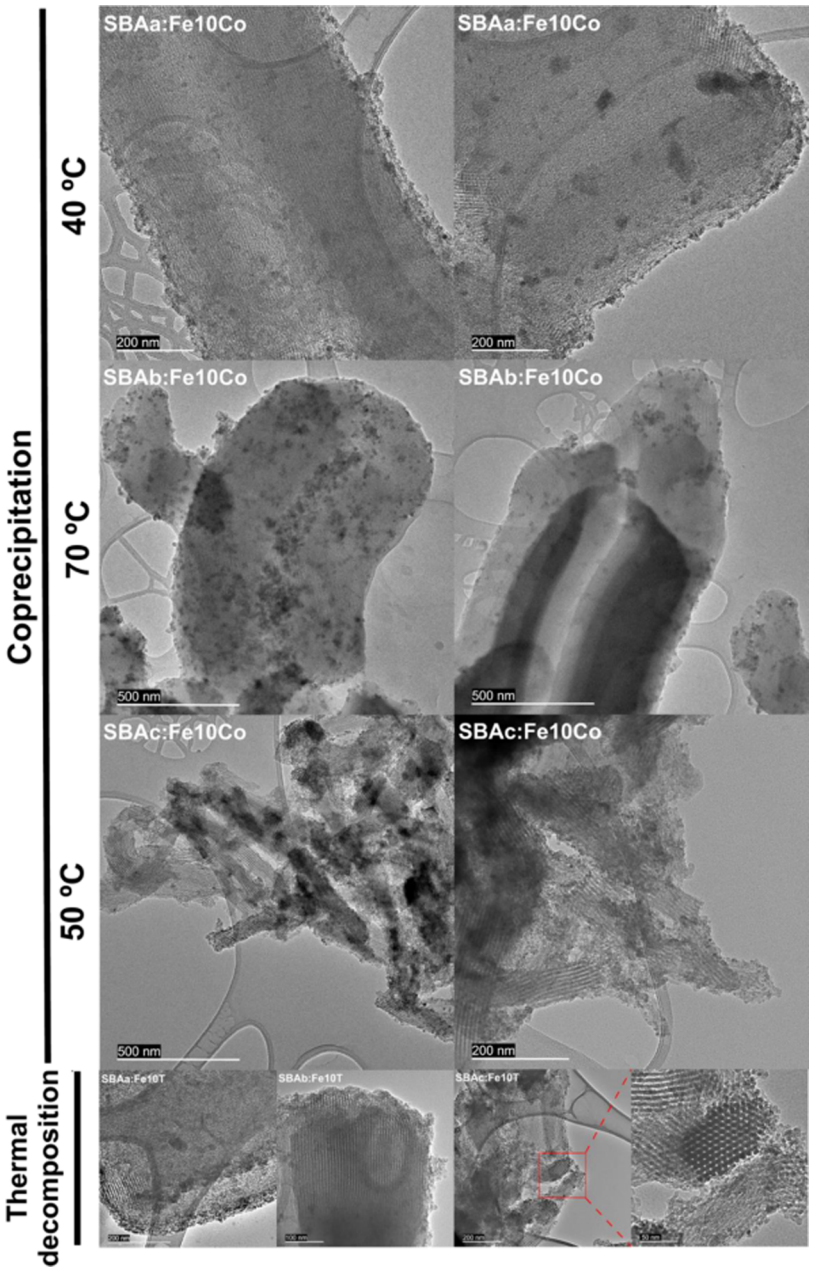

Figure 6. Transmission electron microscopy images of SBA-15:Fe_3O_4 nanocomposites prepared by coprecipitation and thermal decomposition.

morphology of silica (Figure 5). The SBAa prepared by a conventional method consists of uniformly sized particles with an elongated rod shape, formed by aggregates of rods connected as ropelike domains. The particle size and short-rod formation decreased when the synthesis temperature increased from 40 to 70 °C (SBAb). As the synthesis temperature increased from 40 to 50 °C and the stirring rate decreased from 500 to 200 rpm, the particle diameter of the formed silica (SBAc) significantly reduced, with ultrathin nanorods, according to the literature.[43] As shown in Figures 5 and S1 (for SBA-15:Fe_3O_4 nanocomposites with 30 wt % of iron nanoparticles), there are no significant differences in silica morphologies after the inclusion of iron nanoparticles.

Figures S2 and S3 show the EDS spectra of SBA-15:Fe_3O_4 nanocomposites with iron nanoparticles prepared by coprecipitation and thermal decomposition, respectively. All EDS spectra include signals for the main elements, O, Si, and Fe, in the elemental composition of the nanocomposite. Iron peak intensities at 0.7, 6.4, and 7.1 keV, attributed to $Fe_{L\alpha}$, $Fe_{K\alpha 2}$, and $Fe_{K\alpha 1}$, respectively, increased as the iron content increased in the SBA-15:Fe_3O_4 nanocomposites from 10 to 30 wt %, corroborating with data obtained from other analyses, such as SAXS, FTIR, NAI, and thermogravimetric analysis/differential thermal analysis (TGA/DTA). These results confirm that iron nanoparticles were successfully incorporated into the SBA-15 matrix. The EDS mapping of the SBA-15:Fe_3O_4 nanocomposites (Figures S4 and S5) found a homogeneous distribution of the iron nanoparticles in these nanocomposites.

The semiquantitative analysis of the elemental composition (Si, O, and Fe) was obtained from EDS spectra using SEM images, and the graphics of this elemental composition for all SBA-15:Fe_3O_4 nanocomposites, in weight percent, are inserted in Figures S2 and S3. All selected points in the SEM images for EDS analysis presented approximately equal iron content,

https://doi.org/10.1021/acsanm.1c02861
ACS Appl. Nano Mater. 2021, 4, 13363−13378

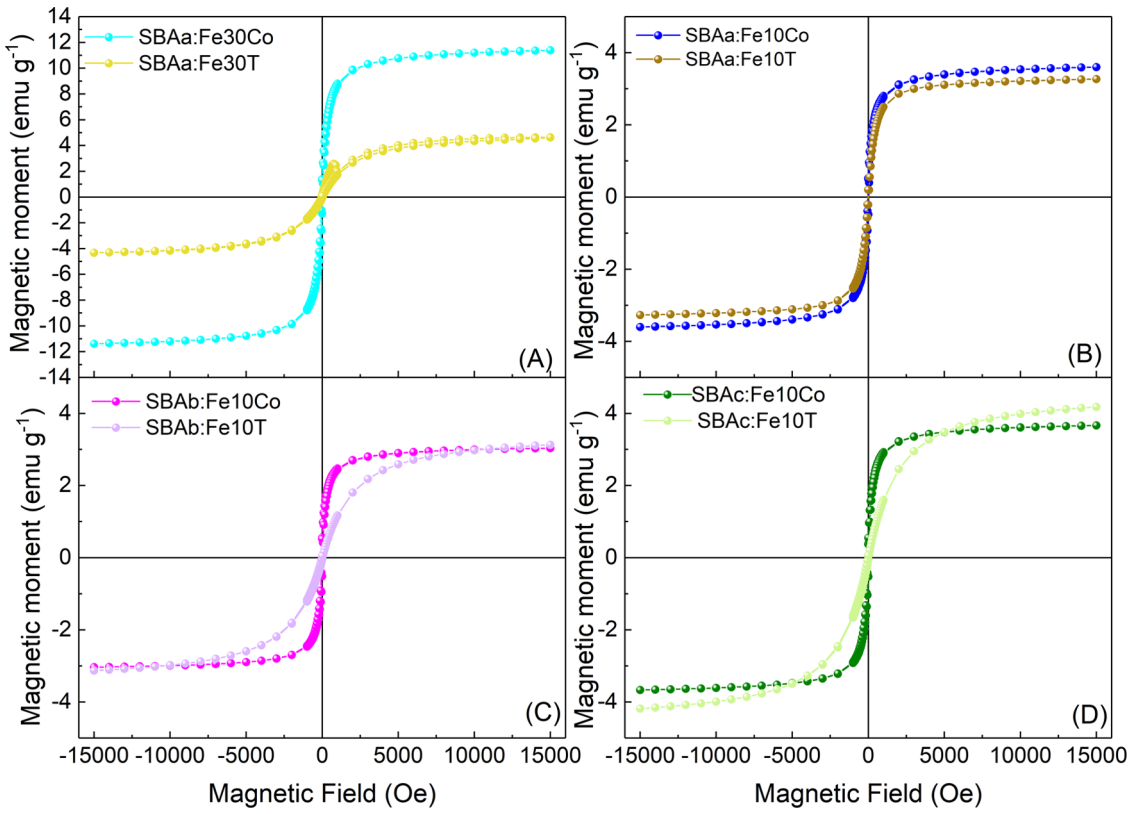

Figure 7. Magnetization curves of SBA-15:Fe_3O_4 nanocomposites. (A) SBAa:Fe30; (B) SBAa:Fe10; (C) SBAb:Fe10; and (D) SBAc:Fe10 nanocomposites, prepared by coprecipitation (Co) and thermal decomposition (T).

indicating the uniform distribution of iron nanoparticles, corroborating the EDS mapping (Figures S4 and S5). The data revealed a similar elemental composition for all nanocomposites with nominal Fe_3O_4 contents of 10 and 30 wt %. The calculated values for iron are about 6 and 19 wt %, corresponding to 8 and 26 wt % of Fe_3O_4, which is lower than the nominal values (10 and 30 wt %) due to their oleic acid coating, in agreement with FTIR and TGA/DTA analysis, which demonstrates the presence of oleic acid in all nanocomposites. The SBAa:Fe30T sample presented a lower iron amount than the SBAa:Fe30Co sample, indicating a higher amount of oleic acid in the first sample, corroborating with the data from the thermogravimetric analysis.

Figure 6 shows the transmission electron microscopy (TEM) micrographs for SBA-15 plus magnetite nanoparticles obtained by both coprecipitation and thermal decomposition methods. In general, micrographs revealed a uniform, rod-shaped morphology with homogeneously distributed magnetite nanoparticles adsorbed on the SBA-15 surface (indicated by arrows in Figure 6). An essential factor is that all temperatures tested for the coprecipitation method resulted in adsorbed Fe_3O_4 nanoparticles with similar spherical morphology and a size interval of ∼7 to 14 nm.

On the other hand, nanoparticles obtained by thermal decomposition method revealed an ultrafine agglomerate appearance, evidenced by the different contrast levels for all temperatures, probably due to the thinner SBA-15 walls at 50 °C (SBAc:Fe10T), compared to the other temperatures of 40 °C (SBAa:Fe10T) and 70 °C (SBAb:Fe10T). Those differences in synthesis methods agree with the size distribution and SEM analysis, as illustrated by the detailed micrography of homogeneous hexagonal SBA-15 mesopore size (with dimensions of ∼6.5 nm) preserved under thermal decomposition.[51]

3.6. Thermal Analysis (TGA/DTA). Figure S6A shows TGA/DTA curves of pure silica (SBAa, SBAb, and SBAc), and Table S2 provides the weight loss percentages of TGA curves and the temperature peaks of those events in DTA curves. There are two weight loss events in the temperature range of 25−900 °C (Figure S6A). The first event (25−160 °C), with weight loss varying between 3 and 8 wt %, accompanied by an endothermic peak around 60 °C (Figure S6B), corresponds to physically adsorbed water release. The second event occurs from 160 to 900 °C and corresponds to the release of silanol groups (4−7 wt %) on the silica surface, accompanied by a broad exothermic peak in DTA curves. These data agree with those reported in the literature.[52]

Figure S7 shows the TGA/DTA curves of SBA-15:Fe_3O_4 nanocomposites, and the weight loss percentages and temperature peaks obtained from these curves are summarized in Table S4. These TGA curves (Figure S7A,C) indicate one weight loss event in the temperature range of 25−170 °C, attributed to the release of physically adsorbed water. The other weight loss events (170−900 °C) correspond to the elimination of silanol groups and the decomposition of the oleic acid, as observed for pure iron nanoparticles. The weight loss in this temperature range increases as the nanoparticles incorporated into the silica matrix increase due to the higher amount of oleic acid-coated iron nanoparticles (from 10 to 30 wt %). All exothermic events attributed to silanol group elimination and oleic acid decomposition observed in DTA curves (Figure S7B,D) agree with those observed in TGA curves. Comparing the residual mass at 900 °C (Table S4) of iron nanoparticles obtained by the thermal decomposition

https://doi.org/10.1021/acsanm.1c02861
ACS Appl. Nano Mater. 2021, 4, 13363−13378

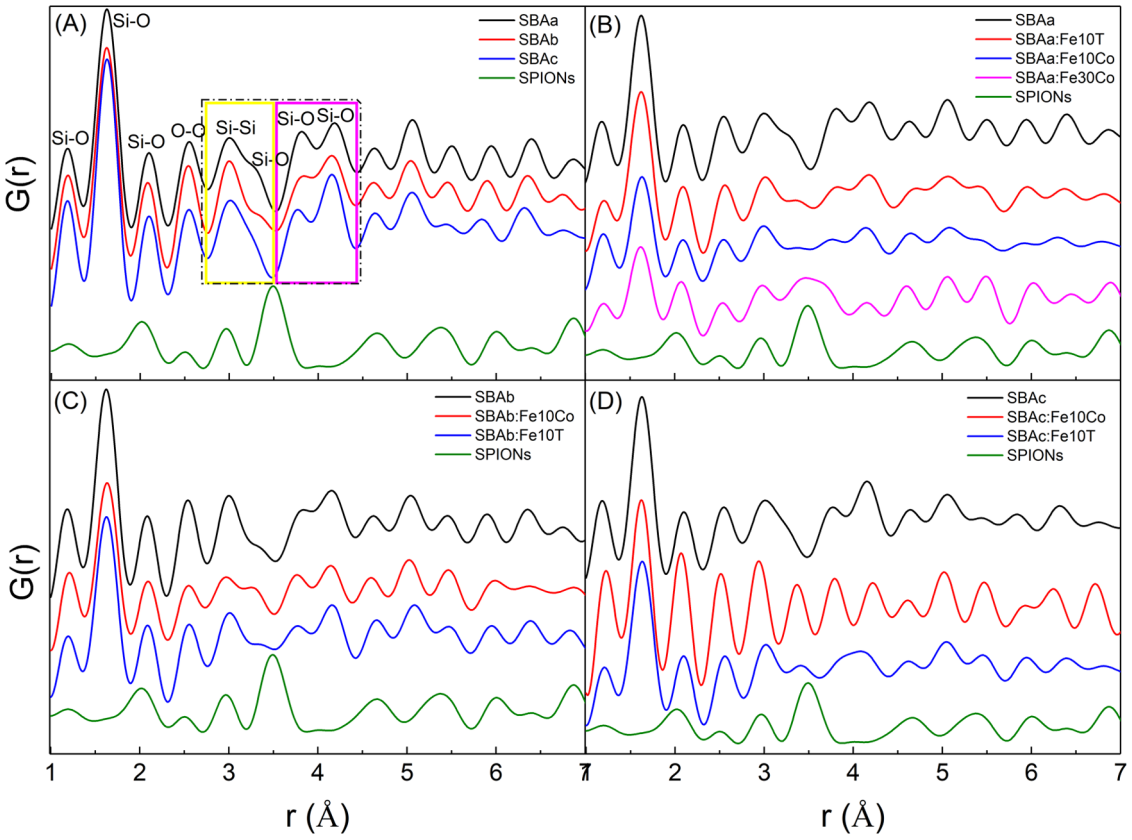

Figure 8. (A) Pair distribution function (PDF) patterns for SBA and pure samples of superparamagnetic iron oxide nanoparticles (SPIONs). (B–D) Comparison between the PDF pattern of SBA-15 and pure SPION samples with nanocomposites samples.

method (SPIONT) with the iron nanoparticles obtained by the coprecipitation method (SPIONCo), the first sample presented lower residual mass than the second samples due to the higher oleic acid content, and this also reflects the SBA-15:Fe_3O_4 nanocomposites. These data corroborate with those observed by other techniques, such as FTIR and EDS analyses.

3.7. Magnetization. Due to the importance of superparamagnetism for the delivery of magnetic targeting nanocarriers, magnetic characterizations were carried out. This property is highly important for the biomedical application of drug-releasing magnetic nanoparticles. Once injected into the blood, these nanoparticles can be guided to the tumor area, for example, by an external magnetic field. This behavior indicates that superparamagnetic nanoparticles can deliver the active compound, such as a therapeutic molecule, directly to the intended target. The magnetization curves of pure iron oxide nanoparticles (SPIONCo and SPIONT) and their respective nanocomposites are displayed in Figures S8 and 7 (A, SBAa:Fe30Co and SBAa:Fe30T; B, SBAa:Fe10Co and SBAa:Fe10T; C, SBAb:Fe10Co and SBAb:Fe10T; and D, SBAc:Fe10Co and SBAc:Fe10T), respectively. Superparamagnetic behavior is evidenced in all samples. The magnetization saturation (MS) values commonly found in the literature for magnetic nanoparticles are usually smaller than those for the corresponding bulk phases, which are ~90 emu g^{-1}.[9,53,54] The lower magnetization value for the nanocomposites confirms the incorporation of SPIONs (10 and 30 wt %) into silica. Nanoparticles are attracted by a magnetic field, and when this field is removed, their magnetization is reduced close to zero, without residual magnetization.[6,55,56] The as-prepared nanoparticles, SPIONT, have a lower magnetic moment than SPIONCo, while in nanocomposites (Figure 7), the magnetic moment does not vary in compounds with the same morphology. Besides avoiding the agglomeration of nanoparticles, this suggests that SBA-15 has mesopores that organize them so that the magnetization of nanoparticles obtained by coprecipitation and thermal decomposition is the same.

The interpretation of the magnetic result is mainly based on the existence of a magnetic core covered by a spin-disordered shell as well as the eventual appearance of other structural phases—hematite or maghemite—on the surface due to the formation of vacancies. Therefore, nanoparticles synthesized in organic solvents (thermal decomposition route) have oleic acid molecules strongly adsorbed on their surface. At the same time, by the coprecipitation method, the magnetic core may be less effectively coated (nonmagnetic layer), leaving the core more exposed and thus increasing the saturation magnetization (Figure S8). The saturation magnetization (MS) values commonly found in our works for magnetic nanoparticles are generally smaller than those of the corresponding bulk phases, which are around 90 emu g^{-1}.[9,53] When the SPIONs are incorporated in the silica, oleic acid is released, and the saturation magnetization of nanocomposites prepared by both methods (T and Co) are similar (Figure 7).

3.8. X-ray Diffraction (XRD) and Pair Distribution Function (PDF). Figure S9 is the X-ray powder diffractograms of the pure SBA-15 and the SBA-15:Fe_3O_4 nanocomposite samples. In all SBA-15-based diffractograms, the amorphous contribution of the SBA-15 system is observed in the q-region of ~1.6 $Å^{-1}$. All of the characteristic peaks of magnetite, Fe_3O_4 (space group $Fd\bar{3}m$, Rietveld refinements in Figure S10),

https://doi.org/10.1021/acsanm.1c02861
ACS Appl. Nano Mater. 2021, 4, 13363−13378

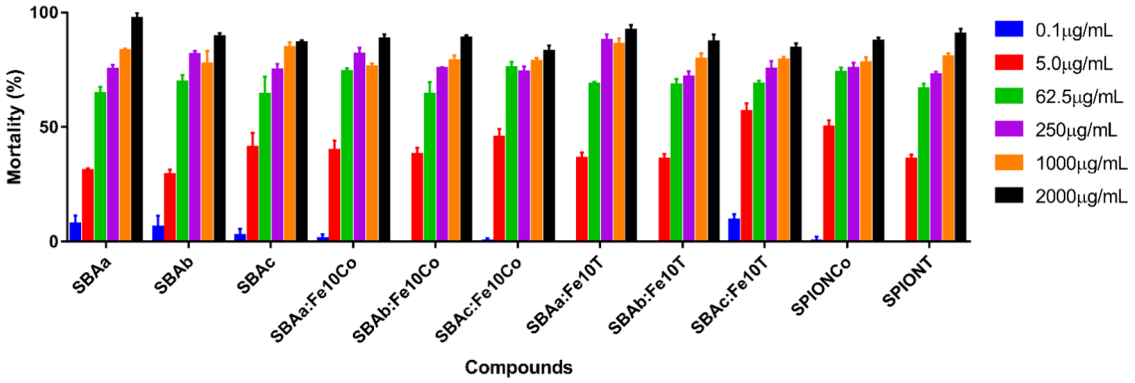

Figure 9. Cell mortality (%) of mononuclear fraction of compounds SBAa, SBAb, SBAc, SBAa:Fe10Co, SBAbFe10Co, SBAc:Fe10Co, SBAa:Fe10CoT, SBAbFe10T, SBAcFe10T, SPINOCo, and SPIONT at 2000, 100, 250, 62.5, 5.0, and 0.1 μg mL^{-1} concentrations.

displayed at the bottom in all diffractograms, are observed in the SBA-15:Fe_3O_4 nanocomposites, indicating the successful incorporation of SPIONs over the SBA-15. We performed Rietveld refinements (Figures S11 and S12) to obtain the unit cell parameters and the crystallite sizes of the SPIONs (Table S5) for all of the nanocomposites. The background was fitted using a Chebyshev polynomial (12 terms), and the peak profiles were modeled using the double Voigt profile model.[57] All of the nanocomposite unit cell parameters are within the standard deviations for all samples and comparable to the pure SPION sample (Table S5). Consistently, the crystallite sizes of the SPIONs synthesized by the thermal decomposition method are smaller than those obtained by the coprecipitation method.

The structure functions for the SBA-15 (a, b, and c) and the SPION pure samples are exhibited in Figure S13. The PDF patterns for the SBAa, SBAb, and SBAc are shown in Figure 8A. The first three peaks around 1.2, 1.6, and 2.1 Å correspond to Si−O distances for the nearest neighbors, and the fourth peak has contributions from O−O pairs. The main difference for the PDF patterns of the SBA-15 pure samples can be seen in the range of 3.5−4.5 Å, and the significant contribution for this region is due to Si−Si (5th peak) and Si−O (6th, 7th, and 8th peaks) correlations, which agrees with results reported by Rantanen et al.[34] related to the description of the SBA-15 structure using the PDF method. These variations also indicate changes in the polymerization degree observed by the SAXS technique, which can lead to the formation of Si−O−Si bonds, i.e., as the degree of polymerization changes, the amount of Si−O−Si can vary accordingly. The region between 3.5 and 4.5 Å encloses the distances between SiO_4 tetrahedrons, and the peaks for the sample SBAa and SBAb are slightly more discriminated up to 3.5 Å (5th and 6th peaks) than the SBAc sample, which suggests a more ordered tetrahedron.[34]

The integral intensity of the PDF peaks is related to the coordination number of pair correlations.[58] In this way, the integral area from 2.7 to 4.2 Å was calculated to evaluate how Si−Si/Si−O correlations contribute to the local ordered structure. The black curve in Figure S14 represents the integral area for the entire region between 2.7 and 4.2 Å, which encloses the Si−Si/Si−O correlations. This region was later divided into two other parts, i.e., from 2.7 to 3.5 Å (yellow square, Figure 8A) and from 3.5 to 4.2 Å (purple square, Figure 8A), to obtain the integral area individually concerned with the contributions of the Si−Si/Si−O and Si−O coordinations, respectively (red and blue curves in Figure S14). As the Si−O coordination decreases, Fe_3O_4 tends to incorporate better over the SBA-15 surface. This can be seen in detail in Figure 8D, where a more disordered distance distribution—in the region near 4 Å—is displayed, following the behavior of the PDF pattern of the SPIONs in this region. Furthermore, the contribution of the highest peak of the SPION sample (near 3.5 Å) is more significant in the nanocomposite samples, which is more evident for the nanocomposite SBAc-based samples than the other ones. For the SBAa:Fe30Co and SBAa:Fe30T samples, with a higher Fe_3O_4 content in the SBA-15 samples, there is a strong contribution in 3.5 Å related to the contribution of SPIONs and more disorder in the region around 4 Å, which agrees with the PDF pattern of SPIONs.

3.9. Biological Assays: Myelotoxicity Assays and Cell Viability of Lymphocyte Assays. The main hematological elements involved in hemostasis processes, such as erythrocytes, platelets, and leukocytes, also perform essential functions in the immune response, which are generally affected by drug treatments and nanomaterials exposition.

As shown in Figure S15, the SBA-15, SPIONs, and nanocomposites (SBA-15:Fe_3O_4) did not induce cytotoxicity other than the reference values (Table S6).[59] These results are essential since the erythrocytes are fundamental cells in the blood of vertebrates, responsible for oxygen transport and other substances to all body tissues (Figure S15A). In the evaluation of red blood cells, we did not find changes in the oxygen transport by hemoglobin present (Figure S15B) in erythrocytes, indicating that compounds with silica and nanoparticles are not myelotoxic, allowing different therapeutic uses by different administration routes.[60−62]

Performance evaluation of platelet count revealed an absence of myelotoxicity in all samples (Figure S15C). Some studies in the literature analyzed the use of silica-based compounds for hemostasis of the hemostatic system, a mechanism responsible for controlling blood loss due to vascular injury.[63−65]

Many studies have investigated the use of compounds with silica for immunological and immunogenic therapy applications since they are currently associated with high toxicity and limited efficacy.[66−68] Therefore, we evaluated the total leukocytes (Figure S15D) from a complete blood count. The compounds did not cause changes in the leukocyte count, revealing that these nanomaterials are promising therapeutic systems.

https://doi.org/10.1021/acsanm.1c02861
ACS Appl. Nano Mater. 2021, 4, 13363−13378

According to the importance of immune function, the viability of healthy leukocytes was evaluated. Most treatments produced similar cell mortality rates near or below 50% at 5 μg mL^{-1} (Figure 9), indicating low toxicity at this concentration, which evidences the concentration potential for new and next tests.

These *in vitro* toxicity results are interesting because they suggest promising applications. These future uses are based on research reporting that these compounds can improve treatments in the proliferation of some cell lines.[69,70]

4. CONCLUSIONS

This detailed study of synthesis and characterization revealed that, although the SBAa and SBAb samples have different morphologies, the silicate tetrahedron (SiO_4) ordering was similar, with a more ordered tetrahedron network structure than the SBAc sample, which has a smaller particle size. The decrease in the Si−O coordination and the low ordering of the silicate tetrahedron for the SBAc were also observed in the PDF results. These data corroborate the nitrogen adsorption isotherms, in which a slight variation in the isotherms profile of the SBAc was observed compared to other two silicas (SBAa and SBAb), which can be attributed to the degree of polymerization that leads to the formation of Si−O−Si bonds due to the higher temperature, combined with the agitation rate that led to a smaller particle size.

No significant changes were observed in the morphological properties of SBA-15:Fe_3O_4 nanocomposites compared to pure SBA-15. However, nanocomposites with the highest SPION content (30 wt %) presented iron oxide nanoparticle agglomeration over the surface of SBA-15, which was higher in the nanocomposites prepared by the coprecipitation method. Although iron oxide nanoparticles were observed on the silica surface, the incorporation of the iron oxide nanoparticles (SPIONCo and SPIONT) into the SBA-15 mesopores was also found. The incorporation was more efficient when SPIONT was used to form the nanocomposites due to its smaller particle size and less polydispersity.

The magnetization curves of SBA-15:Fe_3O_4 nanocomposites are similar, and although the pure SPIONT have lower magnetization than the SPIONs obtained by the coprecipitation method (SBA:Fe10Co), their respective nanocomposites (SBA:Fe10T) presented similar magnetization. However, the SBAc:Fe10T nanocomposites had better magnetization than other nanocomposites (SBAa:Fe10T and SBAb:Fe10T), probably due to the better distribution of the nanoparticles on the silica surface and macroporosity of silica caused by the smaller particle size distribution. However, the same does not happen when the content increases by 30 wt %, which must be related to the agglomeration of iron nanoparticles.

The local structure of the SBA-15:Fe_3O_4 nanocomposites prepared with a lower SPION content (10 wt %) assessed by the PDF method indicated that when the Si−O coordination decreases, better incorporation of the Fe_3O_4 over the SBA-15 surface can be observed. This is evident as the contribution from the PDF pattern of the SPIONs is more pronounced in the nanocomposite samples.

Biological assays, such as myelotoxicity and cell viability, demonstrated that the nanocomposites were safe for potential drug delivery vehicles. These results are impressive because they suggest that these materials can improve some treatments in uncontrolled proliferation.

Furthermore, the work reported by Souza et al.[28] supports the proposition that the nanocomposites developed herein can also be used as drug delivery carriers in addition to their target-carrier characteristics.

The biological assays presented here were performed to determine the best synthesis process to produce the SPIONS. In a future study, new biological tests will be explored to better understand SBA-15:Fe_3O_4 nanocomposites on cells and specific tissues by different model organisms to verify the potential toxicity of these materials. Drug delivery analysis and characterization of these materials after drug delivery will also be carried out.

■ ASSOCIATED CONTENT

Supporting Information

The Supporting Information is available free of charge at https://pubs.acs.org/doi/10.1021/acsanm.1c02861.

Experimental details of the SAXS model for SBA-15, SPIONS, and SBA-15:SPION nanocomposites; size distribution of the SPIONs (Table S1); values of the parameters obtained from the SAXS curves fittings (Table S2); additional SEM images (SBAa:Fe30Co and SBAa:Fe30T nanocomposites); EDS spectra and mapping of all SBA-15:Fe_3O_4 nanocomposites; textural properties (Table S3); thermal analysis results (TGA and DTA curves and data in Table S4); additional magnetization curves; XRD patterns; Rietveld refinement; unit cell parameters and crystallite sizes (Table S5); total structure functions $S(Q)$ for the SBA-15 samples; additional pieces of information of the pair distribution function; and additional biological results (evaluation of cytotoxicity and Table S6) (PDF)

■ AUTHOR INFORMATION

Corresponding Author

Tereza da Silva Martins − *Department of Chemistry, Federal University of São Paulo (UNIFESP), CEP 09913-030 Diadema, SP, Brazil;* orcid.org/0000-0002-7062-5669; Phone: +55-11-40440500; Email: tsmartins@unifesp.br

Authors

Danilo Waismann Losito − *Department of Chemistry, Federal University of São Paulo (UNIFESP), CEP 09913-030 Diadema, SP, Brazil*

Daniele Ribeiro de Araujo − *Center for Human and Natural Sciences (CCNH), Federal University of ABC (UFABC), CEP 09210-580 Santo André, SP, Brazil*

Vinícius Danilo Nonato Bezzon − *Center for Human and Natural Sciences (CCNH), Federal University of ABC (UFABC), CEP 09210-580 Santo André, SP, Brazil*

Pedro Leonidas Oseliero Filho − *Institute of Physics, University of São Paulo, CEP 05508-060 São Paulo, SP, Brazil;* orcid.org/0000-0002-5711-1444

Fernando Luiz Affonso Fonseca − *Faculty of Medicine of ABC—ABC Health University Center, CEP 09060-870 Santo André, SP, Brazil; Department of Pharmaceutical Sciences, Federal University of São Paulo (UNIFESP), CEP 09913-030 Diadema, SP, Brazil*

Camila dos Santos Chagas − *Faculty of Medicine of ABC—ABC Health University Center, CEP 09060-870 Santo André, SP, Brazil*

https://doi.org/10.1021/acsanm.1c02861
ACS Appl. Nano Mater. 2021, 4, 13363−13378

Emerson Barbosa − *Faculty of Medicine of ABC—ABC Health University Center, CEP 09060-870 Santo André, SP, Brazil*

Cristiano Luis Pinto Oliveira − *Institute of Physics, University of São Paulo, CEP 05508-060 São Paulo, SP, Brazil;* orcid.org/0000-0002-3426-6507

Marcia Carvalho de Abreu Fantini − *Institute of Physics, University of São Paulo, CEP 05508-060 São Paulo, SP, Brazil*

Fabio Furlan Ferreira − *Center for Human and Natural Sciences (CCNH), Federal University of ABC (UFABC), CEP 09210-580 Santo André, SP, Brazil;* orcid.org/0000-0003-1516-1221

Paula Silvia Haddad − *Department of Chemistry, Federal University of São Paulo (UNIFESP), CEP 09913-030 Diadema, SP, Brazil*

Complete contact information is available at: https://pubs.acs.org/10.1021/acsanm.1c02861

Notes

The authors declare no competing financial interest.

■ ACKNOWLEDGMENTS

This work was supported by the São Paulo Research Foundation (FAPESP) (processes numbers 17/17844-8 and 2014/50869-6), the Brazilian National Council for Scientific and Technological Development (CNPq) (processes numbers: 465572/2014-6 and 305601/2019-9), and CAPES (Education Ministry) (process number 23038.000776/201754) via the projects of the National Institute for Science and Technology on Organic Electronics (INEO). F.T.A. receives a CAPES fellowship (Finance code 001). P.L.O.F. acknowledges a grant from FAPESP (processes numbers 2019/12301-1 and 2020/13204-7). V.D.N.B. and F.F.F. also thank FAPESP for a grant with process number #2018/11990-5. Thanks go to A.C.F. Silveira and T.M. Germano from the Instituto de Física (USP) and C.M. Fukumoto, R.M. da Silva, R. Rodrigues, and S. Pinheiro from CESM-UNIFESP (Centro de Equipamentos e Serviços Multiusuários do Instituto de Ciências Ambientais). The Brazilian Synchrotron Light Laboratory (LNLS) and Centro Nacional de Pesquisa em Energia e Materiais (CNPEM)/Laboratório Nacional de Nanotecnologia (LNNano) assisted with the TEM images (LNNano: TEM-24450 and TEM-23525). D.R.d.A., F.L.A.F., C.L.P.O., M.C.d.A.F., and F.F.F. are CNPq research fellows.

■ REFERENCES

(1) Rossi, L. M.; Costa, N. J. S.; Silva, F. P.; Wojcieszak, R. Magnetic Nanomaterials in Catalysis: Advanced Catalysts for Magnetic Separation and Beyond. *Green Chem.* **2014**, *16*, 2906−2933.

(2) Long, Y.; Xie, M.; Niu, J.; Wang, P.; Ma, J. Preparation of Acid-Base Bifunctional Core-Shell Structured Fe3O4@SiO2 Nanoparticles and Their Cooperative Catalytic Activity. *Appl. Surf. Sci.* **2013**, *277*, 288−292.

(3) Hu, J.; Chen, G.; Lo, I. M. C. Selective Removal of Heavy Metals from Industrial Wastewater Using Maghemite Nanoparticle: Performance and Mechanisms. *J. Environ. Eng.* **2006**, *132*, 709−715.

(4) Reddy, L. H.; Arias, J. L.; Nicolas, J.; Couvreur, P. Magnetic Nanoparticles: Design and Characterization, Toxicity and Biocompatibility, Pharmaceutical and Biomedical Applications. *Chem. Rev.* **2012**, *112*, 5818−5878.

(5) Stephen, Z. R.; Kievit, F. M.; Zhang, M. Magnetite Nanoparticles for Medical MR Imaging. *Mater. Today* **2011**, *14*, 330−338.

(6) Gonçalves, L. C.; Seabra, A. B.; Pelegrino, M. T.; De Araujo, D. R.; Bernardes, J. S.; Haddad, P. S. Superparamagnetic Iron Oxide Nanoparticles Dispersed in Pluronic F127 Hydrogel: Potential Uses in Topical Applications. *RSC Adv.* **2017**, *7*, 14496−14503.

(7) Gandhi, S.; Venkatesh, S.; Sharma, U.; Jagannathan, N. R.; Sethuraman, S.; Krishnan, U. M. Superparamagnetic Nanosystems Based on Iron Oxide Nanoparticles & Mesoporous Silica: Synthesis & Evaluation of Their Magnetic, Relaxometric and Biocompatibility Properties. *J. Mater. Chem.* **2011**, *21*, 15698−15707.

(8) Khanna, L.; Verma, N. K.; Tripathi, S. K. Burgeoning Tool of Biomedical Applications—Superparamagnetic Nanoparticles. *J. Alloys Compd.* **2018**, *752*, 332−353.

(9) Haddad, P. S.; Duarte, E. L.; Baptista, M. S.; Goya, G. F.; Leite, C. A. P.; Itri, R. Synthesis and Characterization of Silica-Coated Magnetic Nanoparticles. *Prog. Colloid Polym. Sci.* **2004**, *128*, 232−238.

(10) Haddad, P. S.; Martins, T. M.; D'Souza-Li, L.; Li, L. M.; Metze, K.; Adam, R. L.; Knobel, M.; Zanchet, D. Structural and Morphological Investigation of Magnetic Nanoparticles Based on Iron Oxides for Biomedical Applications. *Mater. Sci. Eng., C* **2008**, *28*, 489−494.

(11) Santos, M. C.; Seabra, A. B.; Pelegrino, M. T.; Haddad, P. S. Synthesis, Characterization and Cytotoxicity of Glutathione- and PEG-Glutathione-Superparamagnetic Iron Oxide Nanoparticles for Nitric Oxide Delivery. *Appl. Surf. Sci.* **2016**, *367*, 26−35.

(12) Fudimura, K. A.; Seabra, A. B.; Santos, M. C.; Haddad, P. S. Synthesis and Characterization of Methylene Blue-Containing Silica-Coated Magnetic Nanoparticles for Photodynamic Therapy. *J. Nanosci. Nanotechnol.* **2017**, *17*, 133−142.

(13) Hao, N.; Li, L.; Tang, F. Shape-Mediated Biological Effects of Mesoporous Silica Nanoparticles. *J. Biomed. Nanotechnol.* **2014**, *10*, 2508−2538.

(14) Atashin, H.; Malakooti, R. Magnetic Iron Oxide Nanoparticles Embedded in SBA-15 Silica Wall as a Green and Recoverable Catalyst for the Oxidation of Alcohols and Sulfides. *J. Saudi Chem. Soc.* **2017**, *21*, S17−S24.

(15) Li, Y.-S.; Church, J. S.; Woodhead, A. L.; Moussa, F. Preparation and Characterization of Silica Coated Iron Oxide Magnetic Nano-Particles. *Spectrochim. Acta, Part A* **2010**, *76*, 484−489.

(16) De Witte, K.; Busuioc, A. M.; Meynen, V.; Mertens, M.; Bilba, N.; Tendeloo, G. V.; Cool, P.; Vanant, E. F. Influence of the Synthesis Parameters of TiO2−SBA-15 Materials on the Adsorption and Photodegradation of Rhodamine-6G. *Microporous Mesoporous Mater.* **2008**, *110*, 100−110.

(17) Hoffmann, F.; Cornelius, M.; Morell, J.; Fröba, M. Silica-Based Mesoporous Organic−Inorganic Hybrid Materials. *Angew. Chem., Int. Ed.* **2006**, *45*, 3216−3251.

(18) Li, G.; Zhao, X. S. Characterization and Photocatalytic Properties of Titanium-Containing Mesoporous SBA-15. *Ind. Eng. Chem. Res.* **2006**, *45*, 3569−3573.

(19) Jardim, A. M. L. F.; Bacani, R.; Camilo, F. F.; Fantini, M. C. A.; Martins, T. S. SBA-15:TiO2 Nanocomposites. I. Synthesis with Ionic Liquids and Properties. *Microporous Mesoporous Mater.* **2016**, *228*, 37−44.

(20) Vieira, C. O.; Grice, J. E.; Roberts, M. S.; Haridass, I. N.; Dutra, M. D.; Lopes, P. S.; Leite-Silva, V. R.; Martins, T. S. ZnO:SBA-15 Nanocomposites for Potential Use in Sunscreen: Preparation, Properties, Human Skin Penetration and Toxicity. *Skin Pharmacol. Physiol.* **2018**, *32*, 32−42.

(21) Zhao, D.; Feng, J.; Huo, Q.; Melosh, N.; Fredrickson, G. H.; Chmelka, B. F.; Stucky, G. D. Triblock copolymer syntheses of mesoporous silica with periodic 50 to 300 angstrom pores. *Science* **1998**, *279*, 548−552.

(22) Jardim, A. A.; Bacani, R.; Gonçalves, N. S.; Fantini, M. C. A.; Martins, T. S. SBA-15:TiO2 Nanocomposites: II. Direct and Post-Synthesis Using Acetylacetone. *Microporous Mesoporous Mater.* **2017**, *239*, 235−243.

(23) Zhao, D.; Huo, Q.; Feng, J.; Chmelka, B. F.; Stucky, G. D. Nonionic Triblock and Star Diblock Copolymer and Oligomeric

Surfactant Syntheses of Highly Ordered, Hydrothermally Stable, Mesoporous Silica Structures. *J. Am. Chem. Soc.* **1998**, *120*, 6024−6036.
(24) Martins, T. S.; Mahmoud, A.; Cides, L. C.; Cosentino, I. C.; Tabacniks, M. H.; Matos, J. R.; Freire, R. S.; Fantini, M. C. A. Synthesis, Characterization and Catalytic Evaluation of Cubic Ordered Mesoporous Iron—Silicon Oxides. *Mater. Chem. Phys.* **2010**, *124*, 713−719.
(25) Mirzaei, M.; Zarch, M. B.; Darroudi, M.; Sayyadi, K.; Keshavarz, S. T.; Sayyadi, J.; Fallah, A.; Maleki, H. Silica Mesoporous Structures: Effective Nanocarriers in Drug Delivery and Nanocatalysts. *Appl. Sci.* **2020**, *10*, No. 7533.
(26) Vargas-Osorio, Z.; González-Gómez, M. A.; Piñeiro, Y.; Vázquez-Vázquez, C.; Rodríguez-Abreu, C.; López-Quintela, M. A.; Rivas, J. Novel Synthetic Routes of Large-Pore Magnetic Mesoporous Nanocomposites (SBA-15/Fe3O4) as Potential Multifunctional Theranostic Nanodevices. *J. Mater. Chem. B* **2017**, *5*, 9395−9404.
(27) Aliyan, H.; Fazaeli, R.; Jalilian, R. Fe3O4@mesoporous SBA-15: A magnetically recoverable catalyst for photodegradation of malachite green. *Appl. Surf. Sci.* **2013**, *276*, 147−153.
(28) Souza, K. C.; Ardisson, J. D.; Sousa, E. M. B. Study of Mesoporous Silica / Magnetite Systems in Drug Controlled Release. *J. Mater. Sci. Mater. Med.* **2009**, *20*, 507−512.
(29) Kim, T.; Fu, X.; Warther, D.; Sailor, M. J. Size-Controlled Pd Nanoparticle Catalysts Prepared by Galvanic Displacement into a Porous Si-Iron Oxide Nanoparticle Host. *ACS Nano* **2017**, *11*, 2773−2784.
(30) Billinge, S. J. L.; Kanatzidis, M. G. Beyond Crystallography: The Study of Disorder, Nanocrystallinity and Crystallographically Challenged Materials with Pair Distribution Functions. *Chem. Commun.* **2004**, 749−760.
(31) Petkov, V.; Billinge, S. J. L.; Shastri, S. D.; Himmel, B. Polyhedral Units and Network Connectivity in Calcium Aluminosilicate Glasses from High-Energy X-Ray Diffraction. *Phys. Rev. Lett.* **2000**, *85*, 3436−3439.
(32) Petkov, V.; Difrancesco, R. G.; Billinge, S. J. L.; Acharya, M.; Foley, H. C. Local Structure of Nanoporous Carbons. *Philos. Mag. B* **1999**, *79*, 1519−1530.
(33) Billinge, S. J. L.; Dykhne, T.; Juhás, P.; Božin, E.; Taylor, R.; Florence, A. J.; Shankland, K. Characterisation of Amorphous and Nanocrystalline Molecular Materials by Total Scattering. *CrystEngComm* **2010**, *12*, 1366−1368.
(34) Rantanen, J.; Majda, D.; Riikonen, J.; Lehto, V.-P. The Atomic Local Ordering of SBA-15 Studied with Pair Distribution Function Analysis, and Its Relationship to Porous Structure and Thermal Stability. *Acta Mater.* **2019**, *175*, 341−347.
(35) Oliveira, C. L. P.; Behrens, M. A.; Pedersen, J. S.; Erlacher, K.; Otzen, D.; Pedersen, J. S. A SAXS Study of Glucagon Fibrillation. *J. Mol. Biol.* **2009**, *387*, 147−161.
(36) Brunauer, S.; Emmett, P. H.; Teller, E. Adsorption of Gases in Multimolecular Layers. *J. Am. Chem. Soc.* **1938**, *60*, 309−319.
(37) Barrett, E. P.; Joyner, L. G.; Halenda, P. P. The Determination of Pore Volume and Area Distributions in Porous Substances. I. Computations from Nitrogen Isotherms. *J. Am. Chem. Soc.* **1951**, *73*, 373−380.
(38) Juhás, P.; Davis, T.; Farrow, C. L.; Billinge, S. J. L. PDFgetX3: A Rapid and Highly Automatable Program for Processing Powder Diffraction Data into Total Scattering Pair Distribution Functions. *J. Appl. Crystallogr.* **2013**, *46*, 560−566.
(39) Coelho, A. A. TOPAS and TOPAS-Academic: An Optimization Program Integrating Computer Algebra and Crystallographic Objects Written in C++. *J. Appl. Crystallogr.* **2018**, *51*, 210−218.
(40) Yoffe, S.; Leshuk, T.; Everett, P.; Gu, F. Superparamagnetic iron oxide nanoparticles (spions): synthesis and surface modification techniques for use with MRI and other biomedical applications. *Curr. Pharm. Des.* **2013**, *19*, 493−509.
(41) Luchini, A.; Heenan, R. K.; Paduano, L.; Vitiello, G. Functionalized SPIONs: the surfactant nature modulates the self-assembly and cluster formation. *Phys. Chem. Chem. Phys.* **2016**, *18*, 18441−18449.
(42) Annenkov, V. V.; Danilovtseva, E. N.; Pal'shin, V. A.; Verkhozina, O. N.; Zelinskiy, S. N.; Krishnan, U. M. Silicic Acid Condensation under the Influence of Water-Soluble Polymers: From Biology to New Materials. *RSC Adv.* **2017**, *7*, 20995−21027.
(43) Lee, H. I.; Kim, J. H.; Stucky, G. D.; Shi, Y.; Pak, C.; Kim, J. M. Morphology-Selective Synthesis of Mesoporous SBA-15 Particles over Micrometer, Submicrometer and Nanometer Scales. *J. Mater. Chem.* **2010**, *20*, 8483−8487.
(44) Rubio, F.; Rubio, J.; Oteo, J. L. A FT-IR Study of the Hydrolysis of Tetraethylorthoselicate (TEOS). *Spectrosc. Lett.* **1998**, *31*, 199−219.
(45) Zhang, F.; Yan, Y.; Yang, H.; Meng, Y.; Yu, C.; Tu, B.; Zhao, D. Understanding Effect of Wall Structure on the Hydrothermal Stability of Mesostructured Silica SBA-15. *J. Phys. Chem. B* **2005**, *109*, 8723−8732.
(46) Sundblom, A.; Oliveira, C. L. P.; Palmqvist, A. E. C.; Pedersen, J. S. Modeling in Situ Small-Angle X-ray Scattering Measurements Following the Formation of Mesostructured Silica. *J. Phys. Chem. C* **2009**, *113*, 7706−7713.
(47) Manet, S.; Schmitt, J.; Impéror-Clerc, M.; Zholobenko, V.; Durand, D.; Oliveira, C. L. P.; Pedersen, J. S.; Gervais, C.; Baccile, N.; Babonneau, F.; Grillo, I.; Meneau, F.; Rochas, C. Kinetics of the Formation of 2D-Hexagonal Silica Nanostructured Materials by Nonionic Block Copolymer Templating in Solution. *J. Phys. Chem. B* **2011**, *115*, 11330−11344.
(48) Thommes, M.; Kaneko, K.; Neimark, A. V.; Olivier, J. P.; Rodriguez-Reinoso, F.; Rouquerol, J.; Sing, K. S. W. Physisorption of Gases, with Special Reference to the Evaluation of Surface Area and Pore Size Distribution (IUPAC Technical Report). *Pure Appl. Chem.* **2015**, *87*, 1051−1069.
(49) Kruk, M.; Jaroniec, M.; Ko, C. H.; Ryoo, R. Characterization of the Porous Structure of SBA-15. *Chem. Mater.* **2000**, *12*, 1961−1968.
(50) Ibarra, J.; Melendres, J.; Almada, M.; Burboa, M. G.; Taboada, P.; Juárez, J.; Valdez, M. A. Synthesis and Characterization of Magnetite/PLGA/Chitosan Nanoparticles. *Mater. Res. Express* **2015**, *2*, No. 095010.
(51) Yiu, H. H.; McBain, S. C.; Lethbridge, Z. A.; Lees, M. R.; Palona, I.; Olariu, C.; Dobson, J. Novel Magnetite-Silica Nanocomposite (Fe3O4-SBA-15) Particles for DNA Binding and Gene Delivery Aided by a Magnet Array. *J. Nanosci. Nanotechnol.* **2011**, *11*, 3586−3591.
(52) Cen, S.; Li, W.; He, R.; Tan, J.; Wang, H.; Wei, C.; Tang, Y. Preparation of an Ion Imprinted Functionalized Mesoporous Silica for Rapid and Specific Absorption Cr(III) Ions in Effluents. *RSC Adv.* **2017**, *7*, 37778−37786.
(53) Haddad, P. S.; Seabra, A. B. Biomedical Applications of Magnetic Nanoparticles. In *Iron Oxides: Structure, Properties and Applications*; Martinez, A. I., Ed.; Nova Science Publishers: Nova York, 2012; Vol. *1*, pp 165−188.
(54) Morales, M. A.; Mascarenhas, A. J. S.; Gomes, A. M. S.; Leite, C. A. P.; Andrade, H. M. C.; de Castilho, C. M. C.; Galembeck, F. Synthesis and characterization of magnetic mesoporous particles. *J. Colloid Interface Sci.* **2010**, *342*, 269−277.
(55) Pereira, G. F. L.; Costa, F. N.; Souza, J. A.; Haddad, P. S.; Ferreira, F. F. Parametric Rietveld Refinement and Magnetic Characterization of Superparamagnetic Iron Oxide Nanoparticles. *J. Magn. Magn. Mater.* **2018**, *456*, 108−117.
(56) Toledo, V. K.; Yoshimura, T. M.; Pereira, S. T.; Castro, C. E.; Ferreira, F. F.; Ribeiro, M. S.; Haddad, P. S. Methylene Blue-Covered Superparamagnetic Iron Oxide Nanoparticles Combined with Red Light as a Novel Platform to Fight Non-Local Bacterial Infections: A Proof Of Concept Study Against *Escherichia coli*. *J. Photochem. Photobiol., B* **2020**, *209*, No. 111956.
(57) Coelho, A. A.; Evans, J.; Evans, I.; Kern, A.; Parsons, S. The TOPAS Symbolic Computation System. *Powder Diffr.* **2011**, *26*, S22−S25.

https://doi.org/10.1021/acsanm.1c02861
ACS Appl. Nano Mater. 2021, 4, 13363−13378

(58) Petkov, V.; Difrancesco, R. G.; Billinge, S. J. L.; Acharya, M.; Foley, H. C. Local Structure of Nanoporous Carbons. *Philos. Mag. B* **1999**, *79*, 1519−1530.
(59) ISO 10993-1. *Biological Evaluation of Medical Devices. Part 1: Guidance on Selection of Tests*; International Organization For Standardization: Geneva, 1992.
(60) De La Harpe, K. M.; Kondiah, P. P.; Choonara, Y. E.; Marimuthu, T.; du Toit, L. C.; Pillay, V. The Hemocompatibility of Nanoparticles: A Review of Cell−Nanoparticle Interactions and Hemostasis. *Cells* **2019**, *8*, No. 1209.
(61) Yu, T.; Malugin, A.; Ghandehari, H. Impact of Silica Nanoparticle Design on Cellular Toxicity and Hemolytic Activity. *ACS Nano* **2011**, *5*, 5717−5728.
(62) Bakshi, M. S. Nanotoxicity in Systemic Circulation and Wound Healing. *Chem. Res. Toxicol.* **2017**, *30*, 1253−1274.
(63) Lateef, A.; Ojo, S. A.; Elegbede, J. A.; Akinola, P. O.; Akanni, E. O. Nanomedical Applications of Nanoparticles for Blood Coagulation Disorders. Environ. *Nanotechnology* **2018**, *14*, 243−277.
(64) Zhao, Y.; Sun, X.; Zhang, G.; Trewyn, B. G.; Slowing, I. I.; Lin, V. S.-Y. Interaction of Mesoporous Silica Nanoparticles with Human Red Blood Cell Membranes: Size and Surface Effects. *ACS Nano* **2011**, *5*, 1366−1375.
(65) Pavan, C.; Tomatis, M.; Ghiazza, M.; Rabolli, V.; Bolis, V.; Lison, D.; Fubini, B. In Search of the Chemical Basis of the Hemolytic Potential of Silicas. *Chem. Res. Toxicol.* **2013**, *26*, 1188−1198.
(66) *Adverse Effects of Engineered Nanomaterials: Exposure, Toxicology, and Impact on Human Health*, 2nd ed.; Fadeel, B.; Pietroiusti, A.; Shvedova, A., Eds.; Academic Press: New York, NT, 2017.
(67) Miao, X.; Leng, X.; Zhang, Q. The Current State of Nanoparticle-Induced Macrophage Polarization and Reprogramming Research. *Int. J. Mol. Sci.* **2017**, *18*, No. 336.
(68) Tang, F.; LI, L.; Chen, D. Mesoporous Silica Nanoparticles: Synthesis, Biocompatibility and Drug Delivery. *Adv. Mater.* **2012**, *24*, 1504−1534.
(69) Watermann, A.; Brieger, J. Mesoporous Silica Nanoparticles as Drug Delivery Vehicles in Cancer. *Nanomaterials* **2017**, *7*, No. 189.
(70) Wilhelm, S.; Tavares, A. J.; Dai, Q.; Ohta, S.; Audet, J.; Dvorak, H. F.; Chan, W. C. W. Analysis of Nanoparticle Delivery to Tumours. *Nat. Rev. Mater.* **2016**, *1*, No. 16014.

https://doi.org/10.1021/acsanm.1c02861
ACS Appl. Nano Mater. 2021, 4, 13363−13378